

REDUCED MODELLING OF OSCILLATORY FLOWS IN COMPLIANT CONDUITS AT THE MICROSCALE

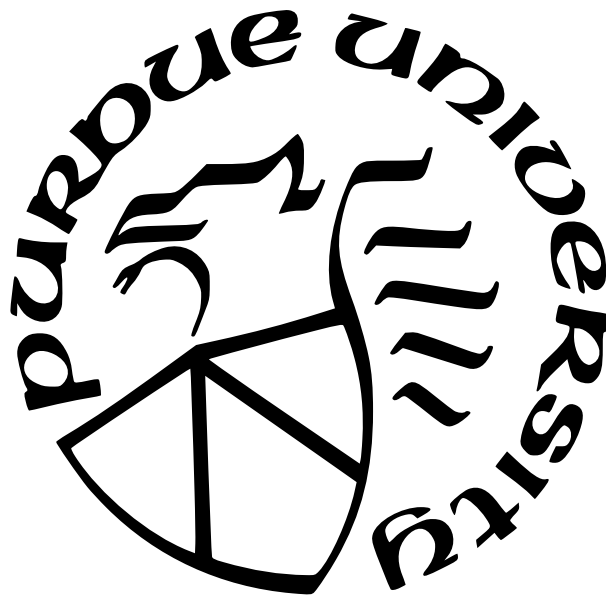
by
Shrihari D. Pande

A Thesis

Submitted to the Faculty of Purdue University

In Partial Fulfillment of the Requirements for the degree of

Master of Science in Mechanical Engineering



School of Mechanical Engineering

West Lafayette, Indiana

May 2023

**THE PURDUE UNIVERSITY GRADUATE SCHOOL
STATEMENT OF COMMITTEE APPROVAL**

Dr. Ivan C. Christov, Chair
School of Mechanical Engineering

Dr. Steven T. Wereley
School of Mechanical Engineering

Dr. Adrian Buganza Tepole
School of Mechanical Engineering

Approved by:
Dr. Nicole L. Key

To my parents

ACKNOWLEDGMENTS

I would like to thank my advisor Prof. Ivan C. Christov for his guidance throughout the work on this project. He took me under his wing during a time of high uncertainty in my life, and I have enjoyed working with him ever since. He is the best mentor and a teacher anyone can ask for and I have cherished every lesson that I have learnt from him.

I would like to thank Xiaojia Wang who helped me get started on this project by agreeing to work with me on developing the theoretical models of this project. Her guidance has been extremely valuable and has helped me develop a greater insight into the mathematical modeling of complex problems.

I would also like to thank Tanmay C. Shidhore for helping me setting up the simulations for the project, Egegeniy Boyko for insightful discussion about lubrication theory and pulsatile flows, as well as the rest of my lab group members Pranay Nagrani and Zongxin Yu for being very welcoming and helping me with numerous things.

Finally, I would like to thank my parents and my sister for their constant moral support throughout my studies.

TABLE OF CONTENTS

LIST OF TABLES	7
LIST OF FIGURES	8
ABSTRACT	9
1 INTRODUCTION	10
1.1 Literature survey on pulsatile flows in microscale fluid–structure interactions	10
1.2 Knowledge gap and organization of the thesis	14
2 OSCILLATORY FLOW IN A TWO-DIMENSIONAL CHANNEL WITH A COMPLIANT TOP WALL	17
2.1 Governing equations: scaling and lubrication approximation	17
2.2 Flow solution at arbitrary Womersley number	18
2.3 Model for the elastic deformation of the channel wall	20
2.4 Reduced model: Governing equation for the pressure	22
2.5 Analytical results	24
2.5.1 Steady flow	24
2.5.2 Weakly deformable channel	24
2.6 Numerical results and discussion	27
3 OSCILLATORY FLOW IN A COMPLIANT 3D AXISYMMETRIC TUBE	31
3.1 Governing equations: scaling and lubrication approximation	31
3.2 Flow solution at arbitrary Womersley number	32
3.3 Model for the elastic deformation of the tube wall	34
3.4 Reduced model: Governing equation for the pressure	35
3.5 Analytical results	36
3.5.1 Steady flow	36
3.5.2 Weakly deformable tube	36
3.6 Numerical results and discussion	39

4	SUMMARY AND OUTLOOK	42
4.1	Thesis summary	42
4.2	Future work	42
	REFERENCES	44

LIST OF TABLES

1.1	Chronological selection of studies on microscale pulsatile flows	13
2.1	Scales for variables for case of a 2D channel	17
2.2	Typical dimensional and dimensionless values of variables and parameters for the case of a 2D channel	19
3.1	Scaling variables for 3D axisymmetric tube	31
3.2	Typical dimensional and dimensionless values of parameters and variables for the case of an axisymmetric tube	33

LIST OF FIGURES

1.1	Picture and schematic of a microfluidic circuit used for flow control	11
1.2	Picture and schematic of a lung-on-a-chip	12
2.1	Schematic of a 2D compliant microchannel, indicating key quantities and notation for the geometry.	18
2.2	Graphs for various numerical and analytical results for a 2D Channel	28
3.1	Schematic of an axisymmetric compliant microtube, indicating key quantities and notation for the geometry.	32
3.2	Graphs for various numerical and analytical results for a 3D axisymmetric tube	40

ABSTRACT

In this thesis, a theory of fluid–structure interaction (FSI) between an oscillatory Newtonian fluid flow and a compliant conduit is developed for canonical geometries consisting of a 2D channel with a deformable top wall and an axisymmetric deformable tube. Focusing on hydrodynamics, a linear relationship between wall displacement and hydrodynamic pressure is employed, due to its suitability for a leading-order-in-slenderness theory. The slenderness assumption also allows the use of lubrication theory, which is used to relate flow rate to the pressure gradient (and the tube/wall deformation) via the classical solutions for oscillatory flow in a channel and in a tube (attributed to Womersley). Then, by two-way coupling the oscillatory flow and the wall deformation via the continuity equation, a one-dimensional nonlinear partial differential equation (PDE) governing the instantaneous pressure distribution along the conduit is obtained, without *a priori* assumptions on the magnitude of the oscillation frequency (i.e., at arbitrary Womersley number). The PDE is solved numerically to evaluate the pressure distribution as well as the cycle-averaged pressure at several points along the length of the channel and the tube. It is found that the cycle-averaged pressure (for harmonic pressure-controlled conditions) deviates from the expected steady pressure distribution, suggesting the presence of a streaming flow. An analytical perturbative solution for a weakly deformable conduit is also obtained to rationalize how FSI induces such streaming. In the case of a compliant tube, the results obtained from the proposed reduced-order PDE and its perturbative solutions are validated against three-dimensional, two-way-coupled direct numerical simulations. A good agreement is shown between theory and simulations for a range of dimensionless parameters characterizing the oscillatory flow and the FSI, demonstrating the validity of the proposed theory of oscillatory flows in compliant conduits at arbitrary Womersley number.

1. INTRODUCTION

1.1 Literature survey on pulsatile flows in microscale fluid–structure interactions

Pulsatile flows in microfluidics, which involves the unsteady flows of fluids at the microscale [1], have a variety of applications in mechanical systems such as the generation of emulsions of droplets, mixing, particle separation, and clog mitigation [2]. One of the most important uses of pulsatile flow in microfluidics involves flow control and shaping, which is used by various *lab-on-a-chip* technologies [3]–[6]. Flow shaping usually involves employing microfluidic circuits consisting of capacitors and diodes (see Fig. 1.1), made of *deformable* elastomers like *polydimethylsiloxane* (PDMS), to ensure an accurate frequency-specific flow response [3]. The capacitors get their name from their ability to store fluid in the deformed bulge, while the diodes permit or obstruct the flows in a particular direction [3]. The flow conduits in both of these components undergo significant deformation. This flow-induced deformation necessitates a thorough understanding of pulsatile flows and the effect of two-way coupled fluid–structure interaction (FSI) on them. The effect on the flow due to the deformable walls must be understood in order to accurately maintain flow control as well as for the design and manufacturing of such devices.

In biological systems, pulsatile flows are essential for enabling bioassay automation, enhancement, or alteration of cell cultures [2]. Pulsatile flows are also omnipresent inside the human body, such as in the form of blood flow through the arteries [7], [8], as well as the flow experienced by endothelial cells of the cardiovascular system, or air flow in and out of the lungs [2], [9]. In recent years, there has been a lot of progress made in the development of *organ-on-a-chip* technologies [10], [11], which like lab-on-a-chip are miniaturized devices used for mimicking the physiology of human organs in a laboratory setting (see Fig. 1.2). These devices also make use of PDMS or other such deformable elastomers. Similar to the flow control chip discussed above, the fluid flow inside the organs and blood vessels is pulsatile and affected by the movement of the vessel or the organ walls, which again makes understanding the two-way coupled FSI of pulsatile flows necessary to accurately mimic the physiology of the human organs.

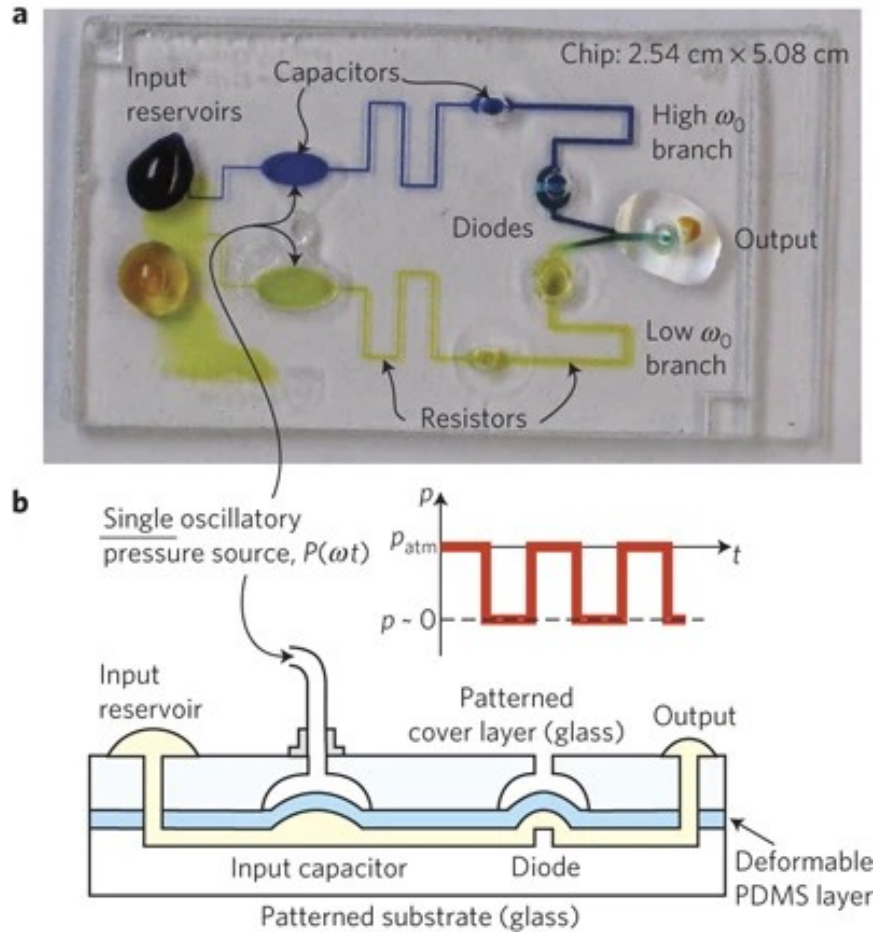


Figure 1.1. An example of a flow control microfluidic circuit with its schematic, which highlights the key components of the circuit. The fluid desired at high frequency is in the upper branch, while the low-frequency fluid is in the lower branch. Both the branches, along with the capacitor and the diode are connected to the single oscillating pressure input. The pressure pulse drives the input capacitor at a controlled frequency, which produces a specific dynamic response in the system. Reproduced with permission from [3] © 2009 Springer Nature.

Several theoretical studies have contributed to the understanding of pulsatile flows in deformable conduits (see Table 1.1). Womersley [12], [13] is credited with the earliest theory of pulsatile flows, including an analytical solution for the velocity profile in a rigid cylindrical tube with a flow driven by a constant, but pulsatile pressure gradient. This theory was then extended to an elastic tube, with the purpose of understanding the physics of blood flow in the arteries. Specifically, Womersley’s theory considered the wall inertia in analyzing the flow,

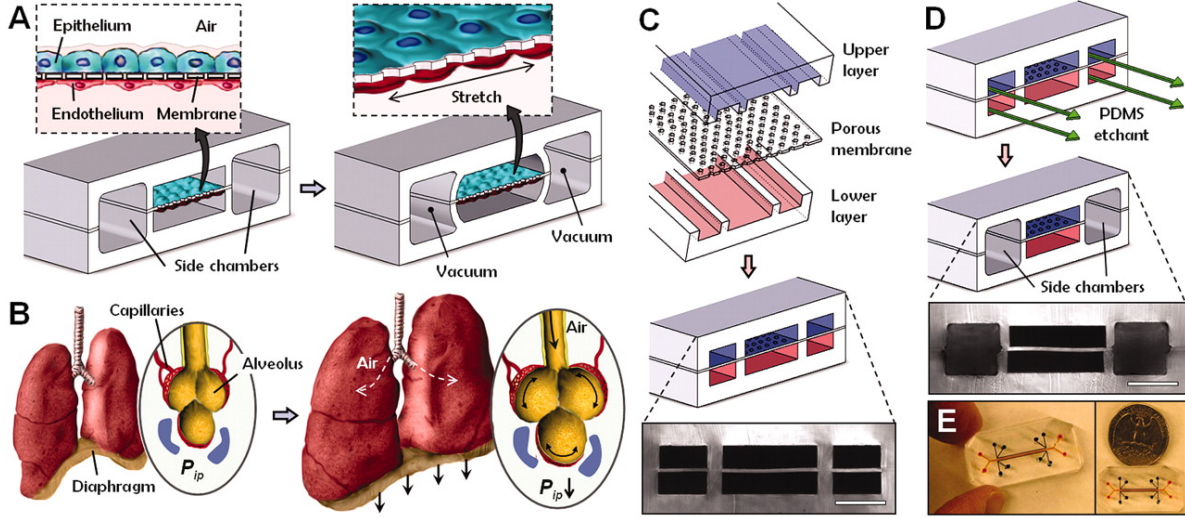


Figure 1.2. An example of a organ-on-a-chip device named lung-on-a-chip, mimicking the breathing process. **A** shows the stretching of the PDMS membrane during inhalation, mimicking the actual behavior of the lung, which is shown in **B**. **C** shows the internal structure of the device. **D** shows the top view of the manufactured microfluidic chip. Reproduced with permission from [10] © 2010 AAAS.

assuming the pressure to be a known sinusoidal function, and did not consider the effect of cross-section deformation on the pressure itself, thus neglecting the two-way coupled effect of the FSI on the flow. Additionally, the deformation was considered to be infinitesimal, thus not changing appreciably the cross-section area of the tube. This assumption has been extensively used in the modeling of lumped parameters (resistance, capacitance, and inductance) for microscale hydraulic systems. In cardiovascular systems, these lumped-parameter models are sometimes known as *windkessel* models [14]. On the other end of the deformation spectrum, Pedley [7] and Grotberg and Jensen [8] reviewed fully coupled FSI modeling of large blood vessels as collapsible tubes with the fluid flow inside them assumed to be in the inertial regime (moderate-to-high Reynolds number). Čanić, Lamponi, Mikelić, *et al.* [15] studied the two-way coupled incompressible viscous flow in a compliant tube and used Greens-function methods to obtain analytical solutions by performing a perturbation expansion in the weak FSI limit. This expansion is sometimes referred to as the ‘domain perturbation approach’.

Table 1.1. A chronological selection of studies on low-Reynolds-number, oscillatory flows in long, slender compliant conduits. Unless otherwise noted, studies involve Newtonian fluids and linearly-elastic walls. Wall inertia is neglected unless otherwise stated. The Womersley number quantifies the order of magnitude of unsteady inertial forces compared to viscous forces. The compliance number quantifies the order of magnitude of the hydrodynamic pressure to the wall’s elastic resistance. The papers classified as “theory” above often also necessitate the numerical solution of a reduced model (as in this thesis).

Reference	Focus	Geometry	Womersley number	Compliance number
Womersley [12], [13]	Theory	Tube	Arbitrary	= 0, wall inertia considered
Čanić, Lamponi, Mikelić, <i>et al.</i> [15]	Theory	Tube	$\mathcal{O}(1)$	$\ll 1$
Čanić, Tambača, Guidoboni, <i>et al.</i> [16]	Theory & experiment, viscoelastic tube	Tube	$\mathcal{O}(1)$	$\ll 1$
Wunderlich, Klefvinger, and Bausch [4]	Theory & experiment	3D channel	$\ll 1$	= 0, lumped-parameter model, deformation seen in experiment
Vedel, Olesen, and Bruus [17]	Theory & experiment	Tube	Arbitrary	= 0, lumped-parameter model
San and Staples [18]	Theory	Tube	Arbitrary	Compliance idealized as slip
Elbaz and Gat [19]	Theory	Tube	$\ll 1$	= 0
Boyko, Bercovici, and Gat [20]	Theory, non-Newtonian fluid	Tube	$\ll 1$	= 0
Kiran Raj, Dasgupta, and Chakraborty [21]	Experiment, non-Newtonian fluid	Tube	0 to 2.17	Unknown, deformation observed
Tulchinsky and Gat [22]	Theory	2D channel	Arbitrary	= 0, wall inertia considered
Anand and Christov [23]	Theory, compressible fluid & viscoelastic tube	Tube	$\ll 1$	$\ll 1$
Vishwanathan and Juarez [24]	Experiment	3D channel	1.5 to 15	No deformation observed
This thesis	Theory & 3D direct simulation	2D channel & Tube	Arbitrary	Not assumed small

Elbaz and Gat [19] studied the effect of oscillatory viscous flow, for low Womersley number, in an elastic tube subject to an external force, while Boyko, Bercovici, and Gat [20] studied the effect of oscillatory non-Newtonian flow in an elastic tube. Both of these studies obtain the governing unsteady equation for the pressure distribution by assuming the deformation to be infinitesimal, thus not changing appreciably the cross-section area of the tube. Tulchinsky and Gat [22] studied the oscillations of a thin film surrounded by the elastic walls excited by a traveling pressure wave, where wall inertia was considered to calculate the frequency response of the film. Like the approach in [19], [20] and Womersley’s solution, this study also did not consider the change in the cross-section area of the channel. On the other hand, Anand and Christov [23] studied compressible fluid flow in a viscoelastic tube in the lubrication limit for low Womersley number with finite compliance of the tube, obtaining perturbation solutions to the two-way coupled problem like in [15].

On the experimental side, Wunderlich, Kleßinger, and Bausch [4] studied the effects of pulsatile flows in a three-dimensional (3D) microchannel and compared the results with a theoretical model comprising of lumped parameters. The theoretical model though was restricted to low Womersley numbers. Vedel, Olesen, and Bruus [17] also made a similar comparison between the lumped-parameter models and experimental results for a tube, but they considered arbitrary Womersley numbers. In both of the latter studies, the effect of two-way coupled FSI was not taken into account in the way the lumped parameters were calculated. Vishwanathan and Juarez [24] also studied pulsatile flow in a 3D channel at sub-kHz frequency but did not report observing any channel deformation. Meanwhile, Kiran Raj, Dasgupta, and Chakraborty [21] studied the effect of non-Newtonian rheology (shear thinning) and reported observing deformation in their experiments, however, their mathematical model does not consider the wall’s compliance.

1.2 Knowledge gap and organization of the thesis

The key knowledge gaps identified from Sec. 1.1 are as follows:

- Despite significant progress being made in the understanding of pulsatile microflows, there is a lack of theory for a two-way coupled pulsatile flow in a deformable conduit in the lubrication limit.
- Many of the studies discussed in Sec. 1.1 assume the pressure to be a known sinusoidal function, or to obey a linear diffusion equation.
- The last assumption neglects the effect of the deformation on the pressure itself, which prevents these theories from capturing the nonlinear pressure gradients experienced by the tubes due to two-way FSI coupling.
- When the effect of FSI was considered (as in [15], [16], [23], for example), the resulting PDEs were expanded in a perturbation for weak FSI. Some of the analytical expressions obtained from the perturbation solution were unwieldy and not of practical use, except in the low Womersley number limit (as in [23]).
- Though experiments have shown significant deformations of the channel or tube during pulsatile low Reynolds number flow [17], [21], a mathematical model of the two-way coupled FSI for such pulsatile flow is absent in the literature.

Realizing that there is a need for understanding pulsatile flows in compliant conduits at arbitrary Womersley numbers, this thesis addresses the above knowledge gaps as follows:

- A reduced 1D model is developed for the canonical geometries of a two-dimensional (2D) channel with a compliant top wall in Chap. 2, and a 3D axisymmetric tube in Chap. 3.
- The velocity profile is obtained at each cross-section by simplifying the Navier–Stokes equation in the lubrication limit. Then, the volumetric flow rate from this oscillatory velocity profile.
- A deformation model based on linear elasticity is used to understand the variation of channel height and tube radius with the pressure in the flow.

- The relations between volumetric flow rate and pressure gradient and pressure and deformation are used to obtain a nonlinear partial differential equation (PDE) for the pressure evolution in a deformable conduit conveying pulsatile flow, ensuring two-way FSI coupling.
- 3D direct numerical simulations are performed to verify the validity of the proposed reduced model (the latter PDE).

For the sake of simplicity, only purely oscillatory flows are discussed, which do not have the mean flow component.

2. OSCILLATORY FLOW IN A TWO-DIMENSIONAL CHANNEL WITH A COMPLIANT TOP WALL

2.1 Governing equations: scaling and lubrication approximation

Consider a two-dimensional (2D) channel in the (y, z) plane as shown in Fig. 2.1. The width w in the spanwise x -direction (into the page, not shown) is so large that the flow may be considered 2D and independent of x . Assume a Newtonian fluid with its dynamic viscosity and density being μ_f and ρ_f , respectively. The flow is driven by an oscillatory pressure (frequency ω , amplitude p_0) imposed at the inlet, and the channel is open to the atmosphere at its outlet. Neglecting any body forces, the mass and momentum conservation equations for this fluid flow [25] are

$$\underbrace{\frac{\partial v_y}{\partial y}}_{\mathcal{O}(1)} + \underbrace{\frac{\partial v_z}{\partial z}}_{\mathcal{O}(1)} = 0, \quad (2.1a)$$

$$\underbrace{\rho_f \frac{\partial v_y}{\partial t}}_{\mathcal{O}(\epsilon^2 \alpha^2)} + \underbrace{\rho_f v_y \frac{\partial v_y}{\partial y}}_{\mathcal{O}(\epsilon^3 Re)} + \underbrace{\rho_f v_z \frac{\partial v_y}{\partial z}}_{\mathcal{O}(\epsilon^2 Re)} = \underbrace{\mu_f \frac{\partial^2 v_y}{\partial y^2}}_{\mathcal{O}(\epsilon^2)} + \underbrace{\mu_f \frac{\partial^2 v_y}{\partial z^2}}_{\mathcal{O}(\epsilon^4)} - \underbrace{\frac{\partial p}{\partial y}}_{\mathcal{O}(1)}, \quad (2.1b)$$

$$\underbrace{\rho_f \frac{\partial v_z}{\partial t}}_{\mathcal{O}(\alpha^2)} + \underbrace{\rho_f v_y \frac{\partial v_z}{\partial y}}_{\mathcal{O}(\epsilon Re)} + \underbrace{\rho_f v_z \frac{\partial v_z}{\partial z}}_{\mathcal{O}(\epsilon Re)} = \underbrace{\mu_f \frac{\partial^2 v_z}{\partial y^2}}_{\mathcal{O}(1)} + \underbrace{\mu_f \frac{\partial^2 v_z}{\partial z^2}}_{\mathcal{O}(\epsilon^2)} - \underbrace{\frac{\partial p}{\partial z}}_{\mathcal{O}(1)}. \quad (2.1c)$$

The scales used to determine the orders of magnitude of terms in Eqs. (3.1) are given in Table 3.1. Three dimensionless numbers (ϵ , Re and α) arise. They are defined in Table 2.2, where their typical values are also given.

Table 2.1. The scales for the variables in the 2D incompressible Navier–Stokes equations (2.1). Note that we have used the lubrication-theory scales for v_y , v_z based on the pressure scale imposed by p_0 [26].

Variable	t	y	z	v_y	v_z	p
Scale	$2\pi/\omega$	h_0	ℓ	$\epsilon \mathcal{V}_z$	$\mathcal{V}_z = \epsilon h_0 p_0 / \mu_f$	p_0

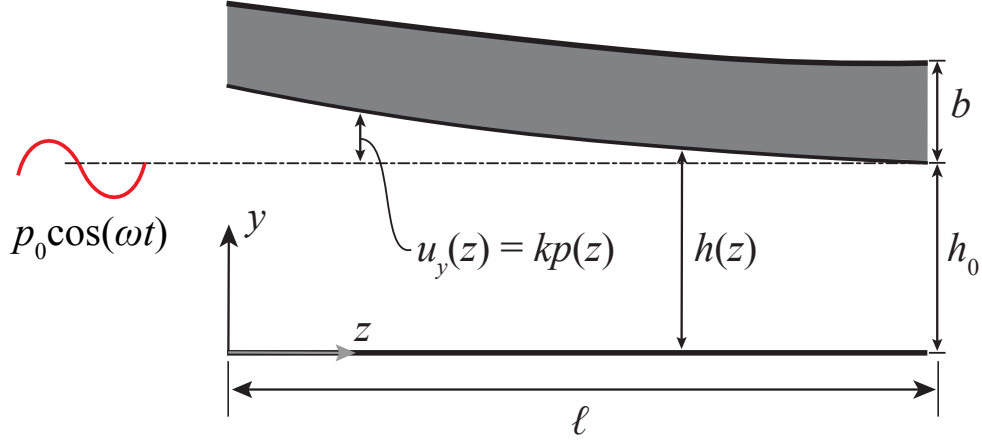


Figure 2.1. Schematic of a 2D compliant microchannel, indicating key quantities and notation for the geometry.

As usual, the Reynolds number Re gauges the order of magnitude of *convective* inertial forces compared to viscous forces. (As discussed in [26], the *effective* Reynolds number ϵRe is actually the relevant quantity herein, on which we make assumptions in Sec. 2.2 below.) Meanwhile, the Womersley number α measures the order of magnitude of *unsteady* inertial forces compared to viscous forces. Although we consider the case of $h = h(z, t)$, we assume that $\max_z h(z, t)$ is always on the order of h_0 , to be consistent with the lubrication approximation, which we now make.

2.2 Flow solution at arbitrary Womersley number

For a microfluidic system of interest, as discussed in Sec. 1.1, Table 2.2 presents the typical values of the relevant dimensional and dimensionless parameters. Thus, we are led to consider the limit of $\epsilon \ll 1$, $\epsilon Re \ll 1$, and $\epsilon^2 \alpha^2 \ll 1$. This limit is the well-known *lubrication approximation* [25], [26], but observe that $\epsilon^2 \alpha^2 \ll 1$ allows the Womersley number α to be $\mathcal{O}(1)$, or even large (say, $\mathcal{O}(\epsilon^{-1})$), within the same approximation. In this regime, Eq. (2.1c) reduces to

$$\rho_f \frac{\partial v_z}{\partial t} = \mu_f \frac{\partial^2 v_z}{\partial y^2} - \frac{\partial p}{\partial z}, \quad (2.2)$$

subject to no slip along the channel walls, $v_z(y = 0, t) = v_z(y = h, t) = 0$. Observe that Eq. (2.2), arising from the lubrication approximation for a deformable channel of variable

Table 2.2. The dimensional and dimensionless parameters of the model for a two-dimensional channel with a compliant wall. The typical fluid is taken to be water, while the typical elastic solid is taken to be polydimethylsiloxane (PDMS), for which $\rho_s \simeq \rho_f$, $\nu_s \simeq 0.5$, and E can be varied. The stiffness constant is estimated as $k = 0.272(1 - \nu_s^2)h_0/E$ [28], while the deformation scale is calculated as $\mathcal{U} = \beta h_0$ (see Sec. 2.4).

Quantity	Notation	Typical value	Units
Channel's length	ℓ	1.0	cm
Channel's undeformed height	h_0	10 to 100	μm
Top wall's thickness	b	10 to 100	μm
Solid's Young's modulus	E	0.1 to 1	MPa
Solid's Poisson's ratio	ν_s	0.49 to 0.5	–
Solid's density	ρ_s	1.0×10^3	kg m^{-3}
Fluid's density	ρ_f	1.0×10^3	kg m^{-3}
Fluid's dynamic viscosity	μ	1.0×10^{-3}	Pa s
Pressure pulse amplitude	p_0	1 to 10	kPa
Pressure pulse frequency	$\omega/2\pi$	1 to 1000	Hz
Channel's height-to-length aspect ratio	$\epsilon = h_0/\ell$	0.001 to 0.01	–
Reynolds number	$Re = \rho_f \epsilon h_0^2 p_0 / \mu_f^2$	0.1 to 100	–
Womersley number	$\alpha = h_0 \sqrt{\rho_f \omega / \mu_f}$	0.03 to 7	–
FSI (or, compliance) number	$\beta = k p_0 / h_0$	0.001 to 0.1	–
Strouhal number	$St = \rho_s b \mathcal{U} \omega^2 / (4\pi^2 p_0)$	$\approx 10^{-9}$ to 10^{-6}	–

height h , is the same as the axial momentum equation in a rigid channel of constant height h_0 , reduced identically for 2D unidirectional flow [25]. Indeed, the channel height h does not have to be constant under the lubrication approximation, as long as it *varies slowly* [27].

Now, if the oscillatory pressure gradient along the channel were separable and time-harmonic, as $-\partial p/\partial z = Ge^{i\omega t}$, then, the post-transient oscillatory flow solution, $v_z(y, t) = f(y)e^{i\omega t}$, to Eq. (2.2) is easily found in complex form (see also [29, p. 89] and the discussion in [30], [31] for several other forms of the solution):

$$v_z(y, t) = \frac{h_0^2}{i\mu_f \alpha^2} \left[1 - \frac{\cos(i^{3/2}(1 - 2y/h)\alpha h/2)}{\cos(i^{3/2}\alpha h/2)} \right] \underbrace{Ge^{i\omega t}}_{\equiv -\partial p/\partial z}. \quad (2.3)$$

The velocity field solution in Eq. (2.3) is given in complex-variable form for convenience, and we may take the real or imaginary part, depending on the boundary conditions. To

introduce α into the solution (2.3), we let $h = h_0\mathfrak{h}$. From Eq. (2.3), the volumetric flow rate is found to be

$$q := \int_0^w \int_0^{h=h_0\mathfrak{h}} v_z \, dy dx = \frac{h_0^3 \mathfrak{h} w}{i\mu_f \alpha^2} \left[1 - \frac{1}{i^{3/2} \alpha \mathfrak{h} / 2} \tan(i^{3/2} \alpha \mathfrak{h} / 2) \right] \left(-\frac{\partial p}{\partial z} \right), \quad (2.4)$$

For oscillatory flow in a rigid channel, $\mathfrak{h} = 1$, $G = G_0$, and Eq. (2.4) can be directly integrated as an ordinary differential equation to find the relationship between the amplitude of the flow rate’s oscillations and the applied pressure gradient’s constant amplitude. For oscillatory flow in a non-uniform (or deformable) channel, however, \mathfrak{h} and G are not constant, so further closures are needed, which we now discuss.

2.3 Model for the elastic deformation of the channel wall

First, we must specify how the height of the channel varies. We are interested in the case of *flow-induced* deformation. Therefore, the channel height varies with the applied load from the hydrodynamic pressure in the channel. This type of channel height variation can generally be expressed as (see, *e.g.*, [28], [32], [33]):

$$h(p) = h_0 + kp = h_0 \underbrace{(1 + kp/h_0)}_{\mathfrak{h}(p)}, \quad (2.5)$$

where k is an effective “stiffness” constant that can be related to the elastic properties of the compliant wall, as well as the geometry [33]. In the context of blood flow in the lungs, Fung [14, Sec. 6.8] uses Eq. (2.5) to model the elasticity of the pulmonary alveolar sheet. The deformation–pressure relation implied by Eq. (2.5), namely $u_y := h - h_0 = kp$, can also be obtained from the reduced deformation model of a 3D microchannel proposed in [28]:

$$\underbrace{\rho_s b \frac{\partial^2 u_y}{\partial t^2}}_{\text{inertia, } \mathcal{O}(St)} + \underbrace{\frac{u_y}{k}}_{\text{stiffness, } \mathcal{O}(1)} - \underbrace{\chi_t \frac{\partial^2 u_y}{\partial z^2}}_{\text{tension, } \mathcal{O}(\theta_t)} + \underbrace{\chi_b \frac{\partial^4 u_y}{\partial z^4}}_{\text{bending, } \mathcal{O}(\theta_b)} = \underbrace{p}_{\text{load, } \mathcal{O}(1)}, \quad (2.6)$$

where b is an (effective) thickness of the fluid–solid interface, which is the same as the thickness of the wall in our analysis, k is the stiffness of the wall, χ_t is the tension per unit

length, and χ_b is the plate-like bending rigidity. Equation (2.6) is also commonly used in models of high-speed flow over compliant coatings (the so-called ‘‘Kramer’s surface’’) [34].

Next, we denote the characteristic scale of u_y as \mathcal{U} and show it can be determined by balancing the surface stiffness term (the second term on the left) with the flow pressure. Let us also introduce $St = \rho_s b \mathcal{U} \omega^2 / (4\pi^2 p_0)$ as the Strouhal number, which represents the (squared) ratio of a characteristic solid deformation time scale ($\sim \sqrt{\rho_s b \mathcal{U} / p_0}$) to the characteristic fluid flow time scale chosen earlier ($2\pi/\omega$) [35]. In the present analysis (as in [28] but unlike [35]), we assume that the wall deformation develops faster than the flow so that $St \ll 1$. Then, the solid inertia is a weak effect, and we neglect it at leading order. We can also write $\chi_t = \bar{E} b \varepsilon_z$ and $\chi_b = \bar{E} b^3 / 12$, where $\bar{E} = E / (1 - \nu_s^2)$, with E and ν_s being the Young’s modulus and the Poisson’s ratio of the solid wall, respectively, and ε_z is the longitudinal strain resulting from either weak pretension or the bulging of the wall. As an example for the latter, for a von Kármán beam, $\varepsilon_z \sim (\mathcal{U}/\ell)^2$ is given in [35]. Assuming that $\mathcal{U} \ll \ell$ and also the compliant top wall is made slender with $b \ll \ell$, it is not difficult to show that $\theta_t = \chi_t \mathcal{U} / (p_0 \ell^2) \sim (b/\ell)(\mathcal{U}/\ell)^3 \ll 1$ and $\theta_b = \chi_b \mathcal{U} / (p_0 \ell^4) \sim (b/\ell)^3 (\mathcal{U}/\ell) \ll 1$, so that the bending and tension are negligible. Then, from Eq. (2.6), we obtain $u_y = kp$ at leading order, so that $\mathcal{U} = \beta h_0$. Here, $\beta := kp_0 / h_0$ is the dimensionless FSI parameter, which gauges the strength of fluid–solid coupling.

Note, however, that though Eq. (2.5) may, on the face of it, appear to be a Winkler-foundation-like model [36] for deformation, no such assumption needs to be made here (see [28]), unlike earlier works [37], [38]. In a ‘‘truly’’ 2D elastic wall, an *incompressible* Winkler-foundation-like model has certain limitations, as discussed in [39]. Having previously derived an ‘‘effective’’ 2D elastic model from a 3D one obviates this issue.

2.4 Reduced model: Governing equation for the pressure

Following the standard procedure (see, *e.g.*, [7], [25], [26]), the conservation of mass equation (2.1a) can be averaged over $y \in [0, h]$, and using the kinematic condition $v_y(y = h, t) = \partial h / \partial t$ yields the continuity equation

$$\frac{\partial q}{\partial z} + \frac{\partial A}{\partial t} = 0, \quad (2.7)$$

where $A = wh(p)$ is the channel's cross-sectional area. On substituting q from Eq. (2.4) and h from Eq. (2.5) into Eq. (2.7), we obtain

$$\frac{h_0^3}{i\mu_f\alpha^2} \frac{\partial}{\partial z} \left\{ -\frac{\partial p}{\partial z} \mathfrak{h}(p) \left[1 - \frac{1}{i^{3/2}\alpha\mathfrak{h}(p)/2} \tan\left(i^{3/2}\alpha\mathfrak{h}(p)/2\right) \right] \right\} + k \frac{\partial p}{\partial t} = 0. \quad (2.8)$$

Next, we introduce dimensionless variables (based on the scales from Table 2.1), denote them by capital letters, and eliminate $\mathfrak{h}(p)$ via Eq. (2.5) from Eq. (2.8), to obtain:

$$\frac{\partial}{\partial Z} \left\{ -\frac{\partial P}{\partial Z} (1 + \beta P) \left[1 - \frac{1}{i^{3/2}\alpha(1 + \beta P)/2} \tan\left(i^{3/2}\alpha(1 + \beta P)/2\right) \right] \right\} + \frac{i\alpha^4\beta}{2\pi\epsilon Re} \frac{\partial P}{\partial T} = 0, \quad (2.9)$$

where $\beta := kp_0/h_0$ has been defined as the FSI (or, compliance) number. The boundary conditions for Eq. (2.9) corresponding to time-harmonic oscillatory flow (driven by a pressure difference along the channel) are

$$P(Z = 0, T) = \cos(2\pi T), \quad (2.10a)$$

$$P(Z = 1, T) = 0. \quad (2.10b)$$

Equation (2.9) is a complex-valued, nonlinear PDE for the pressure distribution $P(Z, T)$ accounting for the oscillatory flow in the 2D channel two-way coupled to the flow-induced deformation of the channel's top elastic wall. Although the PDE (2.9) is based on the long-

time, post-transient flow solution, it still requires an initial condition on P to be marched forward in time. For simplicity, we may impose a zero initial pressure distribution:

$$P(Z, T = 0) = 0, \tag{2.11}$$

and solve the PDE (2.9) for “sufficiently large” T so that this initial condition is “forgotten” and a post-transient state is achieved.

Note that the velocity profile used to obtain the flow rate and the corresponding PDE (2.9) assumes that the pressure gradient is separable as $-\partial p/\partial z = G(z)e^{i\omega t}$, however, the same separation of variable ansatz cannot be used to solve the governing PDE (2.9), owing to its nonlinear nature from two-way coupling of the FSI. This apparent contradiction is resolved by understanding that we have essentially assumed a velocity profile to “close” the cross-sectionally-averaged model. Borrowing the terminology from boundary-layer flows, this closure is generally referred to as the von Kármán–Pohlhausen approximation in a (weakly-)inertial flow in a channel with a deformable wall [28], [32], [35], [40], [41], wherein a steady parabolic profile is used to close the cross-sectionally-averaged momentum equation. (A similar closure problem arises in depth-averaged models of weakly-inertial thin film flows [42, Ch. 6].) Here, we use the unidirectional oscillatory flow solution toward the same goal.

Unfortunately, as is the case with the von Kármán–Pohlhausen approximation, our approximation can only be justified *a posteriori*. In particular in Sec. 3.6, by comparing it to 3D direct numerical simulations. The only other alternative is to consider a weakly deformable conduit and expand the governing equations in $\beta \ll 1$ [15], [16], [23], which is often referred to as the “domain perturbation” approach. However, as Van Dyke [27] argues, the latter approach is expected to have a more limited range of accuracy. Furthermore, even though the resulting linear coupled system of the unsteady mass, momentum, and elasticity equations can be solved analytically at each order in β using, *e.g.*, Green’s function methods [15], [16], the analytical expressions are unwieldy and not of practical use. Meanwhile, our approximation of using the separable oscillatory flow profile to eliminate the momentum equation yields a closed-form reduced-order, two-way coupled FSI model (2.9) that does not assume $\beta \ll 1$ *a priori*.

2.5 Analytical results

From Eq. (2.9), further analytical progress can be made in two distinguished limits, which we now consider.

2.5.1 Steady flow

Diving Eq. (2.9) by $i\alpha^2$ and taking the limit $\alpha \rightarrow 0$, we obtain an ordinary differential equation for the steady pressure distribution in a 2D channel with a deformable wall:

$$\frac{d}{dZ} \left\{ -\frac{dP}{dZ} \left[\frac{1}{12}(1 + \beta P)^3 \right] \right\} = 0. \quad (2.12)$$

With the boundary conditions $P(0) = 1$ and $P(1) = 0$, we obtain the solution for the pressure as:

$$P(Z) = \frac{1}{\beta} \left(\left\{ (1 + \beta)^4 - [(1 + \beta)^4 - 1]Z \right\}^{1/4} - 1 \right). \quad (2.13)$$

As expected [43], the pressure distribution (2.13) is not linear in the deformable channel at steady state ($dP/dZ \neq const.$), but $\lim_{\beta \rightarrow 0} P(Z) = 1 - Z$ as usual.

2.5.2 Weakly deformable channel

Following [15], [16], [23], we can seek a perturbation solution to Eq. (2.9) for weak FSI (*i.e.*, $\beta \ll 1$). To this end, let

$$P(Z, T) = P_0(Z, T) + \beta P_1(Z, T) + \dots. \quad (2.14)$$

Judiciously expanding the nonlinear term within the Z derivative and substituting the expansion from Eq. (2.14) into Eq. (2.9), we obtain:

$$\frac{\partial}{\partial Z} \left\{ -\frac{\partial}{\partial Z} (P_0 + \beta P_1) \left[f_0(\alpha) + \beta (P_0 + \beta P_1) f_1(\alpha) \right] \right\} + \frac{i\alpha^4 \beta}{2\pi\epsilon Re} \frac{\partial (P_0 + \beta P_1)}{\partial T} = 0, \quad (2.15)$$

where, for convenience, we have defined

$$f_0(\alpha) := 1 - \frac{1}{i^{3/2}\alpha/2} \tan(i^{3/2}\alpha/2), \quad (2.16a)$$

$$f_1(\alpha) := -\tan^2(i^{3/2}\alpha/2). \quad (2.16b)$$

Assuming that $\alpha^4\beta/(2\pi\epsilon Re) = \mathcal{O}(\beta)$ asymptotically, collecting $\mathcal{O}(1)$ terms in Eq. (2.15) yields

$$\frac{\partial^2 P_0}{\partial Z^2} = 0 \quad (2.17)$$

subject to

$$P_0(Z = 0, T) = \cos(2\pi T), \quad (2.18a)$$

$$P_0(Z = 1, T) = 0. \quad (2.18b)$$

The solution to the leading-order problem, *i.e.*, Eqs. (2.17) and (2.18), is thus simply:

$$P_0(Z, T) = (1 - Z) \cos(2\pi T). \quad (2.19)$$

Next, collecting $\mathcal{O}(\beta)$ terms in Eq. (2.15) yields

$$f_0(\alpha) \frac{\partial^2 P_1}{\partial Z^2} = -\frac{\partial}{\partial Z} \left[f_1(\alpha) P_0 \frac{\partial P_0}{\partial Z} \right] + \frac{i\alpha^4}{2\pi\epsilon Re} \frac{\partial P_0}{\partial T} \quad (2.20)$$

subject to

$$P_1(Z = 0, T) = 0, \quad (2.21a)$$

$$P_1(Z = 1, T) = 0. \quad (2.21b)$$

The solution for the first-order correction is found, from Eqs. (2.20) and (2.21), to be:

$$P_1(Z, T) = \frac{1}{6} Z(1 - Z) \left[3 \frac{f_1(\alpha)}{f_0(\alpha)} \cos^2(2\pi T) + 2(2 - Z) \frac{i\alpha^4}{2\pi\epsilon Re f_0(\alpha)} \sin(2\pi T) \right]. \quad (2.22)$$

Now, we define the cycle average as

$$\langle \cdot \rangle(Z) := \int_T^{T+1} (\cdot)(Z, T') dT', \quad (2.23)$$

recalling that the dimensionless period is unity in our chosen dimensionless variables. The perturbative, real-valued pressure distribution is then found from Eqs. (2.19) and (2.22) as $\text{Re}[P_0(Z, T)] + \beta \text{Re}[P_1(Z, T)]$. Using the cycle averaging defined in Eq. (2.23), we that the real-valued cycle-averaged pressure is

$$\begin{aligned} \langle P \rangle(Z) &= \text{Re} \left[\underbrace{\langle P_0 \rangle}_{=0} + \beta \langle P_1 \rangle \right] + \mathcal{O}(\beta^2) = \frac{\beta}{4} Z(1-Z) \text{Re} \left[\frac{\mathfrak{f}_1(\alpha)}{\mathfrak{f}_0(\alpha)} \right] + \mathcal{O}(\beta^2) \\ &= \frac{\beta}{4} Z(1-Z) \left(3 - \frac{43}{2100} \alpha^4 \right) + \mathcal{O}(\beta \alpha^8, \beta^2), \end{aligned} \quad (2.24)$$

where we have given the $\alpha \ll 1$ expansion for completeness. Note that we cannot compare the $\alpha \rightarrow 0$ limit of the Eq. (2.24) to the $\beta \ll 1$ expansion of Eq. (2.13) (*i.e.*, the $\alpha \rightarrow 0$ and $\beta \rightarrow 0$ limits do not commute) because in Eq. (2.18a) we imposed a time-dependent boundary condition on P_0 , while P in Eq. (2.13) satisfies a time-independent one. Taking the real part in the expression in Eq. (2.24) has to be done numerically (for plotting and evaluation purposes).

Evidently, Eq. (2.24) implies the existence of a steaming pressure gradient $\partial \langle P \rangle(Z) / \partial Z$, which engenders a non-zero mean flow rate $\langle Q \rangle$. From the dimensionless flow rate corresponding to Eq. (2.4) a lengthy, but straightforward, calculation shows that

$$\begin{aligned} \langle Q \rangle &= -\frac{\beta}{4\alpha^2} \text{Re} [i\mathfrak{f}_1(\alpha)] + \mathcal{O}(\beta^2) \\ &= \frac{\beta}{4\alpha^2} \text{Re} \left[i \tan^2 \left(i^{3/2} \alpha / 2 \right) \right] + \mathcal{O}(\beta^2) = \frac{\beta}{16} \left(1 - \frac{17}{720} \alpha^4 \right) + \mathcal{O}(\beta \alpha^6, \beta^2), \end{aligned} \quad (2.25)$$

which is independent of Z . Further, $\text{Re}[\langle Q \rangle / \beta]$ is a decreasing function for small α and decays to zero as $\alpha \rightarrow \infty$. Interestingly, $\text{Re}[\langle Q \rangle / \beta]$ becomes negative between $\alpha \approx 4.4429$ and $\alpha \approx 8.8858$.

2.6 Numerical results and discussion

The proposed reduced-order model, namely the PDE (2.9), is a non-degenerate nonlinear diffusion equation. However, we need to solve this PDE numerically because, as discussed above, the pressure cannot be assumed to be time-harmonic (as it would be in the classical Womersley-style one-way coupled FSI analysis), and two-way coupling of the flow and deformation leads to a nonlinear PDE. There are many numerical methods suitable for solving such a PDE with ease [44]. For convenience, we simply use the built-in `pdepe` of MATLAB 2020b (Mathworks, Inc.) to solve Eq. (2.9) subject to Eqs. (2.10) and (2.11). `pdepe` uses an auto-generated finite-element spatial discretization of the nonlinear parabolic (or elliptic) PDE provided [44] and the method of lines for time integration, which is accomplished by MATLAB’s adaptive, variable-order multistep stiff solver `ode15s` [45]. The relative tolerance of the solver is set to 10^{-15} , while the absolute tolerance is set to 10^{-8} . A total of 1000 spatial grid points were used. Although Eq. (2.9) is a *complex-valued* PDE, it depends only upon the real variables Z and T , hence it can be solved using `pdepe` just like a real-valued PDE.

An example numerical solution is shown in Fig. 2.2(a) over one cycle of the forcing, after sufficient time has elapsed for the solution to reach a time-periodic state (observe that the P curves at the beginning and end of the cycle shown overlap). By “sufficient time,” we mean that the maximum pressure difference between two consecutive cycles is less than a prescribed tolerance, namely a T such that $\max_Z |P(Z, T) - P(Z, T + 1)| < 10^{-8}$.

Having established a solution procedure for the governing PDE, in Fig. 2.2(b), we next highlight how the pressure distribution obtained from solving Eq. (2.9) numerically varies with the Womersley number, and how it compares to perturbation solution (for the case of $\alpha^2 = 1$ and $\beta = 10^{-3}$). In Fig. 2.2(c), we show the normalized cycled-averaged pressure $\langle P \rangle / \beta$, for the same parameters. The cycle averaged pressure for the numerical solution is calculated using the `trapz` function (trapezoidal rule for integration) in MATLAB, with a dimensionless time-step of $\Delta T = 0.1$, while the cycle averaged pressure from perturbation solution is given by Eq. (2.24). In both Fig. 2.2(b) and 2.2(c), the perturbation solutions

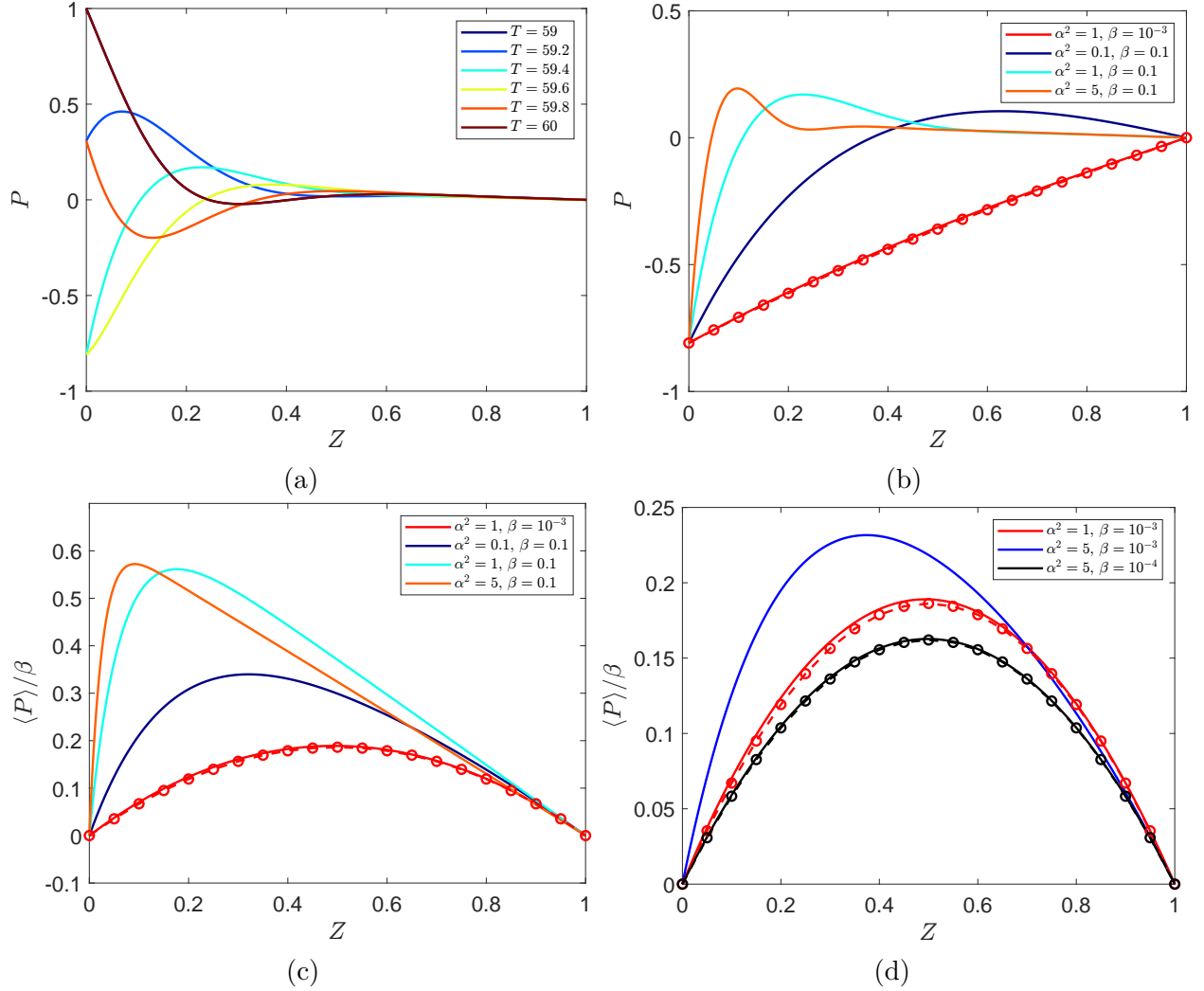


Figure 2.2. (a) The dimensionless pressure distribution at different times, computed by numerically solving Eq. (2.9) subject to Eqs. (2.11) and (2.10) for $\alpha^2 = 1$, $\beta = 0.1$, and $\epsilon Re = 0.01$. (b) The dimensional pressure distribution from (a) at $T = 59.4$ for different values of the Womersley number α and the FSI number β . The dashed curve with circle symbols represents the analytical perturbation solution $\text{Re}[P_0 + \beta P_1]$ found from Eqs. (2.19) and (2.22). (c) The corresponding “universal” normalized streaming pressure $\langle P \rangle / \beta$ profiles. (d) Normalized streaming pressure for $\alpha^2 = 1, 5$ and the effect of FSI parameter (β) on the agreement between the numerical and the perturbative solution. In (c, d), the dashed curves with circle symbols represent the analytical perturbation solution found from Eq. (2.24).

and the numerical solutions are in good agreement with each other, thus demonstrating the utility of the analytical results from Sec. 2.5.2 in the weak FSI regime.

Observe that $\langle P \rangle / \beta$, as calculated in Eq. (2.24) using the perturbation solution, has a “universal” shape with respect to Z , in the sense it only depends solely upon α and no further details of the FSI. The perturbative result agrees very well with the numerical solution, demonstrating that FSI leads to a non-zero pressure despite the inlet forcing having a zero mean. Riley [46] defines *steady streaming* to refer to precisely the latter phenomenon, namely when the “time-average of a fluctuating flow often results in a nonzero mean.”

More generally, viscous streaming refers to the induction of a steady mean flow from time-harmonic oscillations (of the boundaries, inlet conditions, or another mechanism driving the flow). One of the most well-known examples of streaming arises due to small-amplitude, high-frequency oscillations of a body in a viscous (or inviscid) fluid [47], as famously featured in Van Dyke’s *An Album of Fluid Motion* [48, p. 23]. Although classically streaming is induced by the motion of *rigid* objects (or boundaries) in a flow, *soft* streaming has become of interest recently in the context of both external [49] and internal [23] flows. In the context of the present problem of flow in a slender conduit, another classical example of streaming in a viscous flow in a channel is the so-called mechanism of *peristaltic pumping*, which Jaffrin and Shapiro [50] define as “fluid transport that occurs when a progressive wave of area contraction or expansion propagates along the length of a distensible tube containing a liquid.” Traditionally, however, the viscous flow in peristalsis is driven by moving a wavy wall, but Fung and Yih [51] have speculated that peristalsis may be related to the spontaneous oscillations of blood vessels (“vasomotion”), perhaps somewhat akin to the present context in which the conduit walls are not externally actuated.

Earlier work by Hall [52] showed that weak inertia (at the leading order in a suitable Reynolds number) generates a streaming flow when an oscillatory pressure difference is maintained between the ends of a tube of axially varying radius. This phenomenon was successfully analyzed by perturbation expansions for both small and large Womersley number [52]. Recently, however, it was further demonstrated that viscous streaming can arise even a vanishing Reynolds number if the tube radius’ axial variations are due to two-way coupled FSI with the flow [23]. In a sense, FSI self-generates peristaltic pumping without the need of

external intervention (such as moving the wall). However, this zero-Reynolds-number mechanism was only analyzed in [23] at low Womersley numbers and for compressible flow. On the other hand, as our results in this chapter demonstrate, the model proposed in this work is able to capture viscous streaming induced by FSI at an *arbitrary* Womersley number in an incompressible flow.

Finally, returning to Figs. 2.2(c), we observe that the small- β perturbative analytical solution agrees with the numerical solution of the governing PDE only for $\beta \ll 1$ because this assumption was needed to obtain the perturbation solution in Eq. (2.24). Note that, for larger values of the Womersley number, the value of β has to be lowered further to obtain agreement between the perturbation solution and the numerical solution of the PDE. This issue is highlighted in Fig. 2.2(d) for $\alpha^2 = 5$, showing that beta needs to be lowered to $\beta = 10^{-4}$ from $\beta = 10^{-3}$ in order to obtain a good agreement. This change is needed due to the fact that, in deriving the perturbation solution, we assumed that the coefficient of the unsteady pressure term $\propto \alpha^4\beta/(\epsilon Re)$ in Eq. (2.9) is $\mathcal{O}(\beta)$. However, this coefficient's dependence upon α^4 can easily make it $\mathcal{O}(1)$ when $\alpha > 1$. To satisfy the assumptions of our perturbation expansion, we thus have to take $\beta = 10^{-4}$ (for example) when $\alpha^2 = 5$, as evidenced by Fig. 2.2(d)

3. OSCILLATORY FLOW IN A COMPLIANT 3D AXISYMMETRIC TUBE

3.1 Governing equations: scaling and lubrication approximation

Consider a pressure-driven axisymmetric flow without swirl, such that $v_\theta = 0$ and $\partial(\cdot)/\partial\theta = 0$, of a Newtonian fluid in a cylindrical tube with z being the axial direction, as shown in Fig. 3.1. Then, neglecting body forces, the mass and momentum conservation equations for this flow [25] are

$$\underbrace{\frac{1}{r} \frac{\partial}{\partial r} (rv_r)}_{\mathcal{O}(1)} + \underbrace{\frac{\partial v_z}{\partial z}}_{\mathcal{O}(1)} = 0, \quad (3.1a)$$

$$\underbrace{\rho_f \frac{\partial v_z}{\partial t}}_{\mathcal{O}(\alpha^2)} + \underbrace{\rho_f v_r \frac{\partial v_z}{\partial r}}_{\mathcal{O}(\epsilon Re)} + \underbrace{\rho_f v_z \frac{\partial v_z}{\partial z}}_{\mathcal{O}(\epsilon Re)} = \underbrace{\mu_f \frac{1}{r} \frac{\partial}{\partial r} \left(r \frac{\partial v_z}{\partial r} \right)}_{\mathcal{O}(1)} + \underbrace{\mu_f \frac{\partial^2 v_z}{\partial z^2}}_{\mathcal{O}(\epsilon^2)} - \underbrace{\frac{\partial p}{\partial z}}_{\mathcal{O}(1)}, \quad (3.1b)$$

$$\underbrace{\rho_f \frac{\partial v_r}{\partial t}}_{\mathcal{O}(\epsilon^2 \alpha^2)} + \underbrace{\rho_f v_r \frac{\partial v_r}{\partial r}}_{\mathcal{O}(\epsilon^3 Re)} + \underbrace{\rho_f v_z \frac{\partial v_r}{\partial z}}_{\mathcal{O}(\epsilon^3 Re)} = \underbrace{\mu_f \frac{\partial}{\partial r} \left[\frac{1}{r} \frac{\partial}{\partial r} (rv_r) \right]}_{\mathcal{O}(\epsilon^2)} + \underbrace{\mu_f \frac{\partial^2 v_r}{\partial z^2}}_{\mathcal{O}(\epsilon^4)} - \underbrace{\frac{\partial p}{\partial r}}_{\mathcal{O}(1)} \quad (3.1c)$$

The scales used to determine the orders of magnitude of terms in Eqs. (3.1) are given in Table 3.1. Three dimensionless numbers (ϵ , Re and α) arise. Three dimensionless numbers (ϵ , Re and α) arise. They are defined in Table 3.2, where their typical values are also given.

Table 3.1. The scales for the variables in the axisymmetric incompressible Navier–Stokes equations (3.1). We have used the lubrication-theory scales for v_r , v_z based on the pressure scale imposed by p_0 .

Variable	t	r	z	v_r	v_z	p
Scale	$2\pi/\omega$	a_0	ℓ	$\epsilon \mathcal{V}_z$	$\mathcal{V}_z = \epsilon a_0 p_0 / \mu_f$	p_0

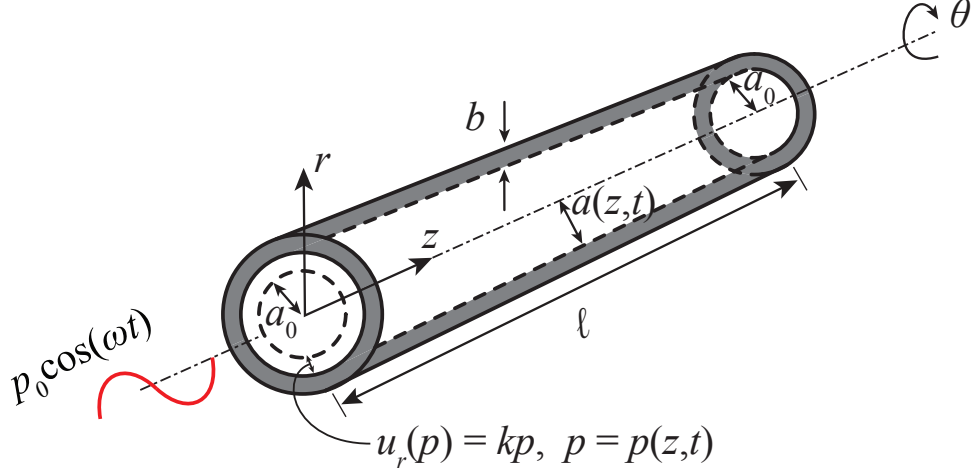


Figure 3.1. Schematic of an axisymmetric compliant microtube, indicating key quantities and notation for the geometry.

3.2 Flow solution at arbitrary Womersley number

Based on the typical values given in Table 3.2, we are led to consider the regime of $\epsilon \ll 1$, $\epsilon Re \ll 1$, $\epsilon^2 \alpha^2 \ll 1$, which reduces Eq. (3.1b) to

$$\rho_f \frac{\partial v_z}{\partial t} = \mu_f \frac{1}{r} \frac{\partial}{\partial r} \left(r \frac{\partial v_z}{\partial r} \right) - \frac{\partial p}{\partial z}, \quad (3.2)$$

subject to no slip along the tube wall, $v_z(r = a, t) = 0$. As before, Eq. (3.2) is valid for arbitrary α^2 (as long as $\epsilon^2 \alpha^2 \ll 1$). As expected, Eq. (3.2) is the same in a rigid tube of constant radius a_0 , as well as a deformable tube of variable radius a . Indeed, the tube radius a does not have to be constant under the lubrication approximation, as long as it *varies slowly* [27]. (In this context, this result was also shown explicitly by Hall [52].)

If the oscillatory pressure gradient along the channel is separable and time-harmonic, as $-\partial p / \partial z = Ge^{i\omega t}$, then, the post-transient oscillatory flow solution, $v_z(r, t) = g(r)e^{i\omega t}$, to Eq. (3.2) is known explicitly from, *e.g.*, Ayyaswamy [54] (credited to Womersley, but also derived earlier by Sexl and contemporaneously by Uchida, see [55, Sec. 4.6]) in complex form:

$$v_z(r, t) = \frac{a_0^2}{i\mu_f \alpha^2} \left[1 - \frac{J_0(i^{3/2} \alpha r / a)}{J_0(i^{3/2} \alpha a)} \right] \underbrace{Ge^{i\omega t}}_{\equiv -\partial p / \partial z}, \quad (3.3)$$

Table 3.2. The dimensional and dimensionless parameters of the model for a compliant microtube. The typical fluid is taken to be water, while the typical elastic solid is taken to be PDMS, for which $\rho_s \simeq \rho_f$, $\nu_s \simeq 0.5$, and E can be varied. The stiffness constant's order of magnitude is estimated as $k = (1 - \nu_s^2)a_0^2/(Eb)$ [53], while the deformation scale is calculated as $\mathcal{U} = \beta a_0$ (see Sec. 3.4).

Quantity	Notation	Typical value	Units
Tube's length	ℓ	1 to 100	mm
Tube's undeformed radius	a_0	0.08 to 0.5	mm
Tube's thickness	b	0.008 to 0.05	mm
Solid's Young's modulus	E	0.5	MPa
Solid's Poisson's ratio	ν_s	0.49 to 0.5	–
Solid's density	ρ_s	1.0×10^3	kg m^{-3}
Fluid's density	ρ_f	1.0×10^3	kg m^{-3}
Fluid's dynamic viscosity	μ_f	1.0×10^{-3}	Pa s
Pressure pulse amplitude	p_0	0.1 to 2	kPa
Pressure pulse frequency	$\omega/2\pi$	1 to 100	Hz
Tube's radius-to-length aspect ratio	$\epsilon = a_0/\ell$	0.002 to 0.06	–
Reynolds number	$Re = \rho_f \epsilon a_0^2 p_0 / \mu_f^2$	2 to 400	–
Womersley number	$\alpha = a_0 \sqrt{\rho_f \omega / \mu_f}$	0.3 to 12	–
FSI (or, compliance) number	$\beta = k p_0 / a_0$	0.005 to 0.1	–
Strouhal number	$St = \rho_s b \mathcal{U} \omega^2 / (4\pi^2 p_0)$	$\approx 10^{-10}$ to 10^{-8}	–

where $J_n(\cdot)$ is the Bessel function of the first kind of order n . To introduce α into the solution (3.3), we let $a = a_0 \mathbf{a}$. As in the 2D case, the solution is given in complex-variable form for convenience, and we may take the real or imaginary part, depending on the boundary conditions. Then, from Eq. (3.3) the flow rate–pressure gradient relation is found to be

$$q(z, t) := 2\pi \int_0^{a=a_0 \mathbf{a}} v_z r dr = \frac{\pi a_0^4 \mathbf{a}^2}{i \mu_f \alpha^2} \left[1 - \frac{2J_1(i^{3/2} \alpha \mathbf{a})}{i^{3/2} \alpha \mathbf{a} J_0(i^{3/2} \alpha \mathbf{a})} \right] \left(-\frac{\partial p}{\partial z} \right). \quad (3.4)$$

For oscillatory flow in a rigid tube, $\mathbf{a} = 1$, $G = G_0$, and Eq. (3.4) can be directly integrated as an ordinary differential equation to find the relationship between the amplitude of the flow rate's oscillations and the applied pressure gradient's constant amplitude. For oscillatory flow in a non-uniform (or deformable) tube, however, \mathbf{a} and G are not constant, so further closures are needed, which we now discuss.

3.3 Model for the elastic deformation of the tube wall

As in Sec. 2.3, the variation of the radius of the tube, due to flow-induced deformation, can generally be expressed as (see, *e.g.*, [19], [33], [53]):

$$a(p) = a_0 + kp = a_0 \underbrace{(1 + kp/a_0)}_{a(p)}, \quad (3.5)$$

where k is again an effective stiffness constant related to the elastic properties of the compliant wall, as well its geometry. In the biofluid mechanics context, Eq. (3.5) is often termed a “tube law” [54], [56]. The deformation–pressure relationship implied by Eq. (3.5), $u_r := a - a_0 = kp$ can be obtained from a suitable shell theory for thin cylindrical structures (see, *e.g.*, [57]). Assuming a long, slender axisymmetric tube, it has been argued in the biomechanics literature (see, *e.g.*, [16] and the numerous references therein and thereof) that linear shell theory generally yields an equation of motion of the form

$$\underbrace{\rho_s b \frac{\partial^2 u_r}{\partial t^2}}_{\text{inertia, } \mathcal{O}(St)} + \underbrace{\frac{u_r}{k}}_{\text{stiffness, } \mathcal{O}(1)} - \underbrace{\chi_t \frac{\partial^2 u_r}{\partial z^2}}_{\text{tension, } \mathcal{O}(\theta_t)} + \underbrace{\chi_b \frac{\partial^4 u_r}{\partial z^4}}_{\text{bending, } \mathcal{O}(\theta_b)} = \underbrace{p}_{\text{load, } \mathcal{O}(1)} \quad (3.6)$$

for the radial displacement u_r , having neglected axial displacements. Here, a Strouhal number is defined as $St = \rho_s b \mathcal{U} \omega^2 / (4\pi^2 p_0)$, and the scale for u_r is again \mathcal{U} .

Next, in the present analysis (as in [19], [20], [58] but unlike [23]), we assume that the wall deformation develops faster than the flow so that $St \ll 1$. Then, the solid inertia is a weak effect, and we neglect it at leading order. As an example, if Eq. (3.6) is derived from linear Koiter shell theory, we have $\chi_t = \bar{E} b^3 \nu_s / (6a_0^2)$ and $\chi_b = \bar{E} b^3 / 12$ (see, *e.g.*, [16]). The use of shell theory requires small strains ($\mathcal{U} \ll \ell$) and a thin ($b \ll a_0$) and slender ($b \ll \ell$) tube. It follows that $\theta_t = \chi_t \mathcal{U} / (p_0 \ell^2) \sim (b/\ell)(b/a_0)^2 (\mathcal{U}/\ell) \ll 1$ and $\theta_b = \chi_b \mathcal{U} / (p_0 \ell^4) \sim (b/\ell)^3 (\mathcal{U}/\ell) \ll 1$, so that the bending and tension are negligible. Then, from Eq. (3.6) we obtain $u_r = kp$ at the leading order, so that $\mathcal{U} = \beta a_0$. (For alternative approaches, starting from the equations of linear elasticity and considering different geometric configurations, boundary conditions, and external loading see [19], [58], [59].)

3.4 Reduced model: Governing equation for the pressure

Following the standard procedure (see, *e.g.*, [7], [25]), the conservation of mass equation (3.1a) for incompressible flow in an axisymmetric deforming tube can be shown to take the same form as the continuity equation for a 2D channel, *i.e.*, Eq. (2.7) (see also [60], [61]). Then, on substituting q from Eq. (3.4) and $A(p) = \pi a(p)^2$ with $a = a_0 \mathbf{a}$ into Eq. (2.7), we obtain

$$\frac{\pi a_0^4}{i\mu_f \alpha^2} \frac{\partial}{\partial z} \left\{ -\frac{\partial p}{\partial z} \mathbf{a}(p)^2 \left[1 - \frac{2J_1(i^{3/2}\alpha \mathbf{a}(p))}{i^{3/2}\alpha \mathbf{a}(p) J_0(i^{3/2}\alpha \mathbf{a}(p))} \right] \right\} + 2\pi(a_0 + kp)k \frac{\partial p}{\partial t} = 0. \quad (3.7)$$

Next, we introduce dimensionless variables (based on the scales from Table 3.1), denote them by capital letters, and eliminate $\mathbf{a}(p)$ via Eq. (3.5) from Eq. (3.7), to obtain:

$$\frac{\partial}{\partial Z} \left\{ -\frac{\partial P}{\partial Z} (1 + \beta P)^2 \left[1 - \frac{2J_1(i^{3/2}\alpha (1 + \beta P))}{i^{3/2}\alpha (1 + \beta P) J_0(i^{3/2}\alpha (1 + \beta P))} \right] \right\} + i \frac{\alpha^4 \beta}{\pi \epsilon Re} (1 + \beta P) \frac{\partial P}{\partial T} = 0, \quad (3.8)$$

where $\beta := kp_0/a_0$ has been defined as the FSI (or, compliance) number. As in Sec. 2.4, for time-harmonic pressure-driven oscillatory flow, the dimensionless initial and boundary conditions for Eq. (3.8) are once again given by Eqs. (2.11) and (2.10), respectively.

Again, we observe that although a separable form of the pressure gradient, in terms of a function of z times a function of t , was used to obtain the flow profile (3.3) from the reduced momentum equation (3.2) and close the relation (3.4) between flow rate and pressure gradient, the final PDE (3.8) for $P(Z, T)$ is nonlinear and, strictly speaking, has no separable solutions. We reconcile this apparent contradiction, as done at the end of Sec. 2.4, by noting that we have essentially used a von Kármán–Pohlhausen-type approximation to close the cross-sectionally-averaged model for oscillatory flow in a deformable conduit. This approximation's validity is checked *a posteriori* in Sec. 3.6 by comparing Eq. (3.8)'s predictions to 3D direct numerical simulations.

3.5 Analytical results

From Eq. (3.8), further analytical progress can be made in two distinguished limits (as in Sec. 2.5), which we now consider.

3.5.1 Steady flow

Diving Eq. (3.8) by $i\alpha^2$ and taking the limit $\alpha \rightarrow 0$, we obtain an ordinary differential equation for the steady pressure distribution in an axisymmetric deformable tube:

$$\frac{d}{dZ} \left[-\frac{dP}{dZ} (1 + \beta P)^4 \right] = 0. \quad (3.9)$$

With the boundary conditions $P(0) = 1$ and $P(1) = 0$, we obtain the solution for the pressure as:

$$P(Z) = \frac{1}{\beta} \left(\left\{ (1 + \beta)^5 - [(1 + \beta)^5 - 1]Z \right\}^{1/5} - 1 \right). \quad (3.10)$$

Observe that the latter is simply the solution for the pressure in a deformable tube in the pressure-controlled regime, complementing the solution for the flow-controlled presented in [53]. As expected [43], the pressure distribution (3.10) is not linear in the deformable tube at steady state ($dP/dZ \neq \text{const.}$), but $\lim_{\beta \rightarrow 0} P(Z) = 1 - Z$ as usual.

3.5.2 Weakly deformable tube

As in Sec. 2.5.2, following [15], [16], [23], let us seek a perturbation solution for weak FSI (*i.e.*, $\beta \ll 1$). Judiciously expanding the nonlinear term within the Z derivative and substituting the expansion from Eq. (2.14) into Eq. (3.8), we obtain:

$$\begin{aligned} \frac{\partial}{\partial Z} \left\{ -\frac{\partial}{\partial Z} (P_0 + \beta P_1) \left[\mathbf{g}_0(\alpha) + \beta (P_0 + \beta P_1) \mathbf{g}_1(\alpha) \right] \right\} \\ + i \frac{\alpha^4 \beta}{\pi \epsilon Re} [1 + \beta (P_0 + \beta P_1)] \frac{\partial}{\partial T} (P_0 + \beta P_1) = 0, \quad (3.11) \end{aligned}$$

where, for convenience, we have defined

$$\mathfrak{g}_0(\alpha) := 1 - \frac{2J_1(i^{3/2}\alpha)}{i^{3/2}\alpha J_0(i^{3/2}\alpha)} = -\frac{J_2(i^{3/2}\alpha)}{J_0(i^{3/2}\alpha)}, \quad (3.12a)$$

$$\mathfrak{g}_1(\alpha) := -\frac{2J_1(i^{3/2}\alpha)^2}{J_0(i^{3/2}\alpha)^2}. \quad (3.12b)$$

Assuming that $\alpha^4\beta/(\pi\epsilon Re) = \mathcal{O}(\beta)$ asymptotically, collecting $\mathcal{O}(1)$ terms in Eq. (3.11) yields

$$\frac{\partial^2 P_0}{\partial Z^2} = 0 \quad (3.13)$$

subject to

$$P_0(Z = 0, T) = \cos(2\pi T), \quad (3.14a)$$

$$P_0(Z = 1, T) = 0. \quad (3.14b)$$

The solution to the leading-order problem, *i.e.*, Eqs. (3.13) and (3.14), is thus simply:

$$P_0(Z, T) = (1 - Z) \cos(2\pi T). \quad (3.15)$$

Next, collecting $\mathcal{O}(\beta)$ terms in Eq. (3.11) yields

$$\mathfrak{g}_0(\alpha) \frac{\partial^2 P_1}{\partial Z^2} = -\frac{\partial}{\partial Z} \left[\mathfrak{g}_1(\alpha) P_0 \frac{\partial P_0}{\partial Z} \right] + i \frac{\alpha^4}{\pi\epsilon Re} \frac{\partial P_0}{\partial T} \quad (3.16)$$

subject to

$$P_1(Z = 0, T) = 0, \quad (3.17a)$$

$$P_1(Z = 1, T) = 0. \quad (3.17b)$$

The solution for the first-order correction is found, from Eqs. (3.16) and (3.17), to be:

$$P_1(Z, T) = \frac{1}{6} Z(1 - Z) \left[3 \frac{\mathfrak{g}_1(\alpha)}{\mathfrak{g}_0(\alpha)} \cos^2(2\pi T) + 2(2 - Z) i \frac{\alpha^4}{\epsilon Re \mathfrak{g}_0(\alpha)} \sin(2\pi T) \right]. \quad (3.18)$$

The perturbative, real-valued pressure distribution is then found from Eqs. (3.15) and (3.18) as $\text{Re}[P_0(Z, T)] + \beta \text{Re}[P_1(Z, T)]$. Finally, using the cycle averaging defined in Eq. (2.23), we find that the real-valued cycle-averaged pressure is

$$\begin{aligned} \langle P \rangle(Z) &= \text{Re}[\underbrace{\langle P_0 \rangle}_{=0} + \beta \langle P_1 \rangle] + \mathcal{O}(\beta^2) = \frac{\beta}{4} Z(1-Z) \text{Re} \left[\frac{\mathbf{g}_1(\alpha)}{\mathbf{g}_0(\alpha)} \right] + \mathcal{O}(\beta^2) \\ &\simeq \frac{\beta}{4} Z(1-Z) \left(4 - \frac{17}{288} \alpha^4 \right) + \mathcal{O}(\beta \alpha^8, \beta^2), \end{aligned} \quad (3.19)$$

where we have given the $\alpha \ll 1$ expansion for completeness. For the same reasons as in Sec. 2.5.2, we cannot compare the $\alpha \rightarrow 0$ limit of the Eq. (3.19) to the $\beta \ll 1$ expansion of Eq. (3.19) (*i.e.*, the $\alpha \rightarrow 0$ and $\beta \rightarrow 0$ limits do not commute). Taking the real part of the expression in Eq. (3.19) has to be done numerically (for plotting and evaluation purposes). Observe that Eq. (3.19) has the same form as Eq. (2.24) for a channel, save for the different dependence on α , highlighting the “universal” nature of the streaming phenomenon in compliant conduits.

Evidently, Eq. (3.19) implies the existence of a steaming pressure gradient $\partial \langle P \rangle(Z) / \partial Z$, which engenders a non-zero mean flow rate $\langle Q \rangle$. From the dimensionless flow rate corresponding to Eq. (3.4), a lengthy, but straightforward, calculation shows that

$$\begin{aligned} \langle Q \rangle &= -\frac{\beta}{4\alpha^2} \text{Re}[\mathbf{i} \mathbf{g}_1(\alpha)] + \mathcal{O}(\beta^2) \\ &= \frac{\beta}{2\alpha^2} \text{Re} \left[\mathbf{i} \frac{J_1(\mathbf{i}^{3/2} \alpha)^2}{J_0(\mathbf{i}^{3/2} \alpha)^2} \right] + \mathcal{O}(\beta^2) = \frac{\beta}{8} \left(1 - \frac{11}{1536} \alpha^4 \right) + \mathcal{O}(\beta \alpha^6, \beta^2), \end{aligned} \quad (3.20)$$

which is evidently independent of Z . Furthermore, unlike 2D channel result in Eq. (2.25), $\text{Re}[\langle Q \rangle / \beta]$ from Eq. (3.20) is a monotonically decreasing function of α , decaying to zero as $\alpha \rightarrow \infty$. As a consistency check, note that the leading $\beta/8$ term in Eq. (2.25) matches the $\alpha = 0$ case analyzed in [23], specifically Eq. (90) therein (upon neglecting wall inertia and fluid compressibility, and simplifying).

3.6 Numerical results and discussion

We performed 3D direct numerical simulation using svFSI, a solver within the open-source cardiovascular modeling software SIMVASCULAR [62], [63]. SvFSI uses the arbitrary Eulerian–Lagrangian framework in the finite element method to solve the two-way coupled FSI problem in a monolithic approach [64]. The large-deformation ‘Saint-Venant–Kirchhoff’ solid model was used in svFSI. The 3D, unsteady incompressible Navier–Stokes equations are solved in the fluid domain, without the assumption of axisymmetry. Following [59], the simulation was set up by creating a cylindrical fluid domain surrounded by an elastic solid mesh representing a thin tube, maintaining an aspect ratio of $\epsilon = 0.0667$. For the simulations, a conforming unstructured mesh was used for each of the fluid and solid domains, with a combined 160,859 tetrahedral elements, which was created in the commercial software ANSYS and converted to a format compatible with svFSI. An oscillatory input was given by a time-varying boundary condition at the inlet, specifically a cosine variation of the pressure, whose amplitude was matched to yield $\beta = 0.06$ and whose frequency was matched to yield the desired value of α . (Note that, since we are considering a thin elastic tube, β does not have to be too large to observe nonlinear effects due to FSI, and indeed it cannot be too large before nonlinear deformations of the tube itself emerge; see the discussion in [53].)

Three different simulations corresponding to Womersley numbers $\alpha^2 = 0.1, 1, \text{ and } 5$ were performed with a time step of 10^{-6} s for 60 periods of the forcing. The simulation data was saved in dimensionless time steps of $\Delta T = 0.1$, which is the same interval used to compute the cycle-averaged pressure. An additional simulation for $\alpha^2 = 1$ with $\beta = 0.001$ and $\epsilon = 0.0667$ was performed to compare the results with the perturbation solution, which requires different dimensionless parameters to ensure its validity (the weakly deformable regime).

As in Sec. 2.6, the proposed reduced-order model (3.8) for the pressure, which we remind is valid for $\beta = \mathcal{O}(1)$ (having taken into account two-way FSI coupling), is solved numerically in MATLAB using `pdepe` using the same settings as before. Upon obtaining the numerical solution, we take its real part and compare it to the direct numerical simulation from svFSI. To enable this comparison, the 3D pressure solution from svFSI is averaged across several

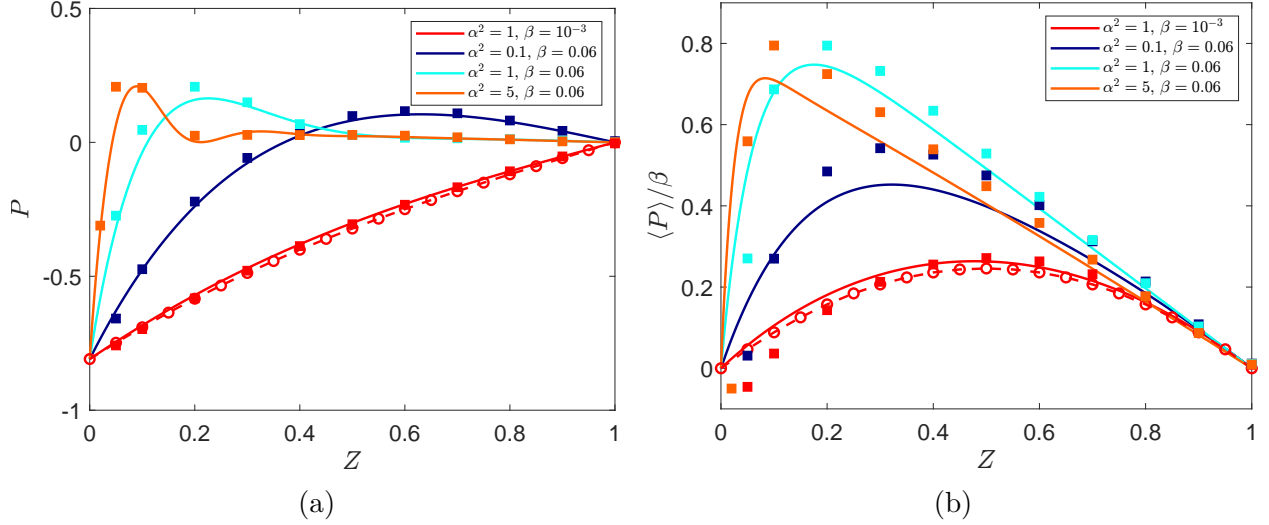


Figure 3.2. (a) The dimensionless pressure distribution at the non-dimensional time of $T = 59.4$. Symbols denote the results from svFSI simulations, while curves denote the numerical solution of Eq. (3.8) subject to Eqs. (2.11) and (2.10). The dashed curve with circle symbols represents the analytical perturbation solution $\text{Re}[P_0 + \beta P_1]$ found from Eqs. (3.15) and (3.18). (b) The ‘universal’ normalized streaming pressure $\langle P \rangle / \beta$ profile for different values of the Womersley number α and the FSI number β . Symbols denote the results from svFSI simulations, while the curves denote the numerical solution of Eq. (3.8). The dashed curve with circle symbols represents the analytical perturbation solution from Eq. (3.19).

different cross-sections along the length of the tube and made dimensionless using the scales from Table 3.1.

In Fig. 3.2(a), the pressure distribution obtained from the numerical solution of Eq. (3.8) is compared with the simulation data obtained from svFSI, for different Womersley numbers, at the dimensionless time of $T = 59.4$. We observe good agreement between the instantaneous pressure profiles from the reduced model and the 3D simulations. The perturbative analytical solution from Eqs. (3.15) and (3.18) is also shown for a Womersley number of $\alpha^2 = 1$. In Fig. 3.2(b), the corresponding normalized streaming pressure profile, $\langle P \rangle / \beta$ computed again in MATLAB using `trapz` with a dimensionless time step of $\Delta T = 0.1$, obtained from 3D svFSI simulations, the `pdepe` solution of Eq. (3.8), and the perturbation solution from Eq. (3.19), are shown and compared for different values of the Womersley number. We find a good agreement between all three, thus demonstrating the validity of the proposed the-

ory of oscillatory flows in compliant conduits at arbitrary Womersley number. As discussed in Sec. 3.5.2, the perturbative result is valid only for $\beta \ll 1$ such that $\alpha^4\beta/(\pi\epsilon Re) = \mathcal{O}(\beta)$, thus it is only shown for $\alpha^2 = 1$ and $\beta = 10^{-3}$ in Fig. 3.2. However, the numerical solution of Eq. (3.8) accurately captures both the pressure variation in Fig. 3.2(a) and the normalized streaming pressure trend in Fig. 3.2(b), demonstrating that the proposed model in this work is able to capture viscous streaming induced by FSI at an *arbitrary* Womersley number in an incompressible flow.

4. SUMMARY AND OUTLOOK

4.1 Thesis summary

This thesis developed a theory of two-way coupled fluid-structure interaction for deformable conduits undergoing oscillatory flows. Specifically, two canonical geometries comprising a 2D channel and a 3D axisymmetric tube undergoing flow due to an oscillatory pressure gradient were considered in chapters 2 and 3, respectively. The velocity profile and the subsequent flow rate for each of the geometries were evaluated in the lubrication limit of the flow and were used as an approximation to close the momentum equation, similar to the von Kármán–Pohlhausen approximation used in boundary layer theory. A simple deformation model based on linear elasticity was introduced to characterize the variation of the channel height and the tube radius with the hydrodynamic pressure in the oscillatory flow. The deformation equation, along with the flow rate were substituted into the mass conservation equation to obtain a nonlinear PDE governing the pressure evolution, ensuring a two-way coupled FSI model. The proposed PDE was solved numerically and an analytical perturbative solution of the same PDE, in a weak FSI limit, was obtained to ensure and demonstrate its applicability in the said limit. A cycle-averaged pressure was also evaluated from both the numerical and perturbation solutions, which showed the mean pressure profile deviating from the steady one. Thus, it was concluded that a streaming flow was induced by the coupling between oscillatory flow and channel or tube deformation due to FSI. Additionally, for the case of the tube in chapter 3, a 3D direct numerical simulation was performed in the open-source finite-element solver svFSI. The direct numerical simulations showed a good agreement with the numerical and perturbative solutions of the reduced 1D model, thus validating our proposed PDE for the pressure evolution in deformable conduits undergoing oscillatory flows.

4.2 Future work

Although this thesis focused on purely oscillatory flows, the proposed reduced model can be extended to understand pulsatile flows which include an added mean flow component on

top of the oscillating component by simply changing boundary conditions of the PDE, *e.g.*, Eq. (3.8).

The proposed reduced model can also be extended to accurately model microfluidic hydraulic systems by calculating new expressions for the lumped parameters of the circuit. As discussed in Sec. 3.1, the windkessel models used in the modeling of cardiovascular systems include a number of assumptions such as a negligible change in the cross-section area of the conduit (thus, in a way, they are ‘linearized’). As explained by Morris and Forster [65] when such approximate lumped parameters were compared with experiments, it resulted in a 400% error in the frequency response. As also explained in [65], the lumped parameter should be derived from the full flow solutions, or in the present case from the solution of the two-way coupled FSI problem. Hence, in future work, it can be explored if the reduced models from this thesis can rectify some issues regarding hydraulic compliance, and perhaps explain some observed experimental results.

The validity of the reduced model proposed in this thesis could further be tested by comparing it with the experiments. Additionally, a 3D direct numerical simulation using svFSI can be performed for other geometries of interest, such as the ones described in the review [33] or the recent paper [59].

On the mathematical side, in future work, it would be of interest to re-evaluate the perturbation solutions in the distinguished limit in which the unsteady term in Eqs. (2.15) and (3.11) is not neglected at $\mathcal{O}(\beta^0)$. This would extend the scope of analytical solutions for larger values of the FSI parameter, thus ensuring greater applicability of the proposed model.

Finally, more work can be done to further justify the von Kármán–Pohlhausen-type approximation for velocity made in Chap. 2, Eq. (2.3) and Chap. 3, Eq. (3.3). Right now, the assumption can only be justified *a posteriori*. A more mathematically justifiable reasoning would enhance the case for using such approximations in deriving reduced 1D models for more complex, deformable microfluidic systems experiencing pulsatile flow.

REFERENCES

- [1] N.-T. Nguyen and S. T. Wereley, *Fundamentals and Applications of Microfluidics* (Integrated Microsystems Series), 2nd. Norwood, MA: Artech House, 2006.
- [2] B. Dincau, E. Dressaire, and A. Sauret, “Pulsatile Flow in Microfluidic Systems,” *Small*, vol. 16, p. 1904032, 2020. DOI: [10.1002/smll.201904032](https://doi.org/10.1002/smll.201904032).
- [3] D. C. Leslie, C. J. Easley, E. Seker, *et al.*, “Frequency-specific flow control in microfluidic circuits with passive elastomeric features,” *Nat. Phys.*, vol. 5, pp. 231–235, 2009. DOI: [10.1038/NPHYS1196](https://doi.org/10.1038/NPHYS1196).
- [4] B. K. Wunderlich, U. A. Kleßinger, and A. R. Bausch, “Diffusive spreading of time-dependent pressures in elastic microfluidic devices,” *Lab Chip*, vol. 10, pp. 1025–1029, 2010. DOI: [10.1039/b920221h](https://doi.org/10.1039/b920221h).
- [5] R. R. Collino, N. Reilly-Shapiro, B. Foresman, *et al.*, “Flow switching in microfluidic networks using passive features and frequency tuning,” *Lab Chip*, vol. 13, pp. 3668–3674, 2013. DOI: [10.1039/C3LC50481F](https://doi.org/10.1039/C3LC50481F).
- [6] M. D. Biviano, M. V. Paludan, A. H. Christensen, E. V. Østergaard, and K. H. Jensen, “Smoothing Oscillatory Peristaltic Pump Flow with Bioinspired Passive Components,” *Phys. Rev. Applied*, vol. 18, p. 064013, 2022. DOI: [10.1103/PhysRevApplied.18.064013](https://doi.org/10.1103/PhysRevApplied.18.064013).
- [7] T. J. Pedley, *The Fluid Mechanics of Large Blood Vessels*. Cambridge: Cambridge University Press, 1980. DOI: [10.1017/CBO9780511896996](https://doi.org/10.1017/CBO9780511896996).
- [8] J. B. Grotberg and O. E. Jensen, “Biofluid mechanics in flexible tubes,” *Annu. Rev. Fluid Mech.*, vol. 36, pp. 121–147, 2004. DOI: [10.1146/annurev.fluid.36.050802.121918](https://doi.org/10.1146/annurev.fluid.36.050802.121918).
- [9] J. B. Grotberg, “Pulmonary flow and transport phenomena,” *Annu. Rev. Fluid Mech.*, vol. 26, pp. 529–571, 1994. DOI: [10.1146/annurev.fl.26.010194.002525](https://doi.org/10.1146/annurev.fl.26.010194.002525).
- [10] D. Huh, B. D. Matthews, A. Mammoto, M. Montoya-Zavala, H. Y. Hsin, and D. E. Ingber, “Reconstituting organ-level lung functions on a chip,” *Science*, vol. 328, pp. 1662–1668, 2010. DOI: [10.1126/science.1188302](https://doi.org/10.1126/science.1188302).
- [11] S. N. Bhatia and D. E. Ingber, “Microfluidic organs-on-chips,” *Nat. Biotechnol.*, vol. 32, pp. 760–772, 2014. DOI: [10.1038/nbt.2989](https://doi.org/10.1038/nbt.2989).

- [12] J. R. Womersley, “XXIV. Oscillatory motion of a viscous liquid in a thin-walled elastic tube—I: The linear approximation for long waves,” *Phil. Mag., Ser. 7*, vol. 46, pp. 199–221, 1955. DOI: [10.1080/14786440208520564](https://doi.org/10.1080/14786440208520564).
- [13] J. R. Womersley, “An Elastic Tube Theory of Pulse Transmission and Oscillatory Flow in Mammalian Arteries,” Wright Air Development Center, Wright-Patterson AFB, OH, Tech. Rep. TR 56-614, 1957. [Online]. Available: <https://apps.dtic.mil/sti/citations/ADB295267>.
- [14] Y. C. Fung, *Biomechanics: Circulation*, 2nd ed. New York, NY: Springer-Verlag, 1997. DOI: [10.1007/978-1-4757-2696-1](https://doi.org/10.1007/978-1-4757-2696-1).
- [15] S. Čanić, D. Lamponi, A. Mikelić, and J. Tambača, “Self-consistent effective equations modeling blood flow in medium-to-large compliant arteries,” *Multiscale Model. Simul.*, vol. 3, pp. 559–596, 2005. DOI: [10.1137/030602605](https://doi.org/10.1137/030602605).
- [16] S. Čanić, J. Tambača, G. Guidoboni, A. Mikelić, C. J. Hartley, and D. Rosenstrauch, “Modeling Viscoelastic Behavior of Arterial Walls and Their Interaction with Pulsatile Blood Flow,” *SIAM J. Appl. Math.*, vol. 67, pp. 164–193, 2006. DOI: [10.1137/060651562](https://doi.org/10.1137/060651562).
- [17] S. Vedel, L. H. Olesen, and H. Bruus, “Pulsatile microfluidics as an analytical tool for determining the dynamic characteristics of microfluidic systems,” *J. Micromech. Microeng.*, vol. 20, p. 035 026, 2010. DOI: [10.1088/0960-1317/20/3/035026](https://doi.org/10.1088/0960-1317/20/3/035026).
- [18] O. San and A. E. Staples, “Dynamics of pulsatile flows through elastic microtubes,” *Int. J. Appl. Mech.*, vol. 4, p. 1 250 006, 2012. DOI: [10.1142/S175882511200135X](https://doi.org/10.1142/S175882511200135X).
- [19] S. B. Elbaz and A. D. Gat, “Dynamics of viscous liquid within a closed elastic cylinder subject to external forces with application to soft robotics,” *J. Fluid Mech.*, vol. 758, pp. 221–237, 2014. DOI: [10.1017/jfm.2014.527](https://doi.org/10.1017/jfm.2014.527).
- [20] E. Boyko, M. Bercovici, and A. D. Gat, “Viscous-elastic dynamics of power-law fluids within an elastic cylinder,” *Phys. Rev. Fluids*, vol. 2, p. 073 301, 2017. DOI: [10.1103/PhysRevFluids.2.073301](https://doi.org/10.1103/PhysRevFluids.2.073301).
- [21] M. Kiran Raj, S. Dasgupta, and S. Chakraborty, “Biomimetic pulsatile flows through flexible microfluidic conduits,” *Biomicrofluidics*, vol. 13, p. 014 103, 2019. DOI: [10.1063/1.5065901](https://doi.org/10.1063/1.5065901).

- [22] A. Tulchinsky and A. D. Gat, “Frequency response and resonance of a thin fluid film bounded by elastic sheets with application to mechanical filters,” *J. Sound Vib.*, vol. 438, pp. 83–98, 2019. DOI: [10.1016/j.jsv.2018.08.047](https://doi.org/10.1016/j.jsv.2018.08.047).
- [23] V. Anand and I. C. Christov, “Transient compressible flow in a compliant viscoelastic tube,” *Phys. Fluids*, vol. 32, p. 112 014, 2020. DOI: [10.1063/5.0022406](https://doi.org/10.1063/5.0022406).
- [24] G. Vishwanathan and G. Juarez, “Generation and application of sub-kilohertz oscillatory flows in microchannels,” *Microfluid. Nanofluid.*, vol. 24, p. 69, 2020. DOI: [10.1007/s10404-020-02373-z](https://doi.org/10.1007/s10404-020-02373-z).
- [25] R. L. Panton, *Incompressible Flow*, 4th. Hoboken, NJ: John Wiley & Sons, 2013. DOI: [10.1002/9781118713075](https://doi.org/10.1002/9781118713075).
- [26] H. A. Stone, “Fundamentals of fluid dynamics with an introduction to the importance of interfaces,” in *Soft Interfaces*, ser. Lecture Notes of the Les Houches Summer School, L. Bocquet, D. Quéré, T. A. Witten, and L. F. Cugliandolo, Eds., vol. 98, New York, NY: Oxford University Press, 2017, pp. 3–79. DOI: [10.1093/oso/9780198789352.003.0001](https://doi.org/10.1093/oso/9780198789352.003.0001).
- [27] M. Van Dyke, “Slow variations in continuum mechanics,” *Adv. Appl. Mech.*, vol. 25, pp. 1–45, 1987. DOI: [10.1016/S0065-2156\(08\)70276-X](https://doi.org/10.1016/S0065-2156(08)70276-X).
- [28] X. Wang and I. C. Christov, “Reduced modelling and global instability of finite-Reynolds-number flow in compliant rectangular channels,” *J. Fluid Mech.*, vol. 950, A26, 2022. DOI: [10.1017/jfm.2022.802](https://doi.org/10.1017/jfm.2022.802).
- [29] L. D. Landau and E. M. Lifshitz, *Fluid Mechanics* (Course of Theoretical Physics), 2nd. Oxford: Pergamon Press, 1987, vol. 6. DOI: [10.1016/C2013-0-03799-1](https://doi.org/10.1016/C2013-0-03799-1).
- [30] J. Majdalani, “Exact Navier-Stokes Solution for the Pulsatory Viscous Channel Flow with Arbitrary Pressure Gradient,” *J. Propuls. Power*, vol. 24, pp. 1412–1423, 2008. DOI: [10.2514/1.37815](https://doi.org/10.2514/1.37815).
- [31] S. Tabakova, N. Kutev, and S. Radev, “Oscillatory Carreau flows in straight channels,” *R. Soc. Open Sci.*, vol. 7, p. 191 305, 2020. DOI: [10.1098/rsos.191305](https://doi.org/10.1098/rsos.191305).
- [32] X. Wang and I. C. Christov, “Reduced models of unidirectional flows in compliant rectangular ducts at finite Reynolds number,” *Phys. Fluids*, vol. 33, p. 102 004, 2021. DOI: [10.1063/5.0062252](https://doi.org/10.1063/5.0062252).

- [33] I. C. Christov, “Soft hydraulics: from Newtonian to complex fluid flows through compliant conduits,” *J. Phys.: Condens. Matter*, vol. 34, p. 063001, 2022. DOI: [10.1088/1361-648X/ac327d](https://doi.org/10.1088/1361-648X/ac327d).
- [34] J. J. Riley, M. Gad-el-Hak, and R. W. Metcalfe, “Compliant coatings,” *Annu. Rev. Fluid Mech.*, vol. 20, pp. 393–420, 1988. DOI: [10.1146/annurev.fl.20.010188.002141](https://doi.org/10.1146/annurev.fl.20.010188.002141).
- [35] T. C. Inamdar, X. Wang, and I. C. Christov, “Unsteady fluid-structure interactions in a soft-walled microchannel: A one-dimensional lubrication model for finite Reynolds number,” *Phys. Rev. Fluids*, vol. 5, p. 064101, 2020. DOI: [10.1103/PhysRevFluids.5.064101](https://doi.org/10.1103/PhysRevFluids.5.064101).
- [36] D. A. Dillard, B. Mukherjee, P. Karnal, R. C. Batra, and J. Frechette, “A review of Winkler’s foundation and its profound influence on adhesion and soft matter applications,” *Soft Matter*, vol. 14, pp. 3669–3683, 2018. DOI: [10.1039/c7sm02062g](https://doi.org/10.1039/c7sm02062g).
- [37] J. M. Skotheim and L. Mahadevan, “Soft Lubrication,” *Phys. Rev. Lett.*, vol. 92, p. 245509, 2004. DOI: [10.1103/PhysRevLett.92.245509](https://doi.org/10.1103/PhysRevLett.92.245509).
- [38] X. Yin and S. Kumar, “Lubrication flow between a cavity and a flexible wall,” *Phys. Fluids*, vol. 17, p. 063101, 2005. DOI: [10.1063/1.1914819](https://doi.org/10.1063/1.1914819).
- [39] T. G. J. Chandler and D. Vella, “Validity of Winkler’s mattress model for thin elastomeric layers: beyond Poisson’s ratio,” *Proc. R. Soc. A*, vol. 476, p. 20200551, 2020. DOI: [10.1098/rspa.2020.0551](https://doi.org/10.1098/rspa.2020.0551).
- [40] P. S. Stewart, S. L. Waters, and O. E. Jensen, “Local and global instabilities of flow in a flexible-walled channel,” *Eur. J. Mech. B/Fluids*, vol. 28, pp. 541–557, 2009. DOI: [10.1016/j.euromechflu.2009.03.002](https://doi.org/10.1016/j.euromechflu.2009.03.002).
- [41] R. Borcia, M. Bestehorn, S. Uhlig, M. Gaudet, and H. Schenk, “Liquid pumping induced by transverse forced vibrations of an elastic beam: A lubrication approach,” *Phys. Rev. Fluids*, vol. 3, p. 084202, 2018. DOI: [10.1103/PhysRevFluids.3.084202](https://doi.org/10.1103/PhysRevFluids.3.084202).
- [42] S. Kalliadasis, C. Ruyer-Quil, B. Scheid, and M. G. Velarde, *Falling Liquid Films* (Applied Mathematical Sciences). London: Springer, 2012, vol. 176. DOI: [10.1007/978-1-84882-367-9](https://doi.org/10.1007/978-1-84882-367-9).
- [43] S. I. Rubinow and J. B. Keller, “Flow of a viscous fluid through an elastic tube with applications to blood flow,” *J. Theor. Biol.*, vol. 34, pp. 299–313, 1972. DOI: [10.1016/0022-5193\(72\)90041-0](https://doi.org/10.1016/0022-5193(72)90041-0).

- [44] R. D. Skeel and M. Berzins, “A Method for the Spatial Discretization of Parabolic Equations in One Space Variable,” *SIAM J. Sci. Stat. Comput.*, vol. 11, pp. 1–32, 1990. DOI: [10.1137/0911001](https://doi.org/10.1137/0911001).
- [45] L. F. Shampine and M. W. Reichelt, “The MATLAB ODE Suite,” *SIAM J. Sci. Comput.*, vol. 18, pp. 1–22, 1997. DOI: [10.1137/S1064827594276424](https://doi.org/10.1137/S1064827594276424).
- [46] N. Riley, “Steady streaming,” *Annu. Rev. Fluid Mech.*, vol. 33, pp. 43–65, 2001. DOI: [10.1146/annurev.fluid.33.1.43](https://doi.org/10.1146/annurev.fluid.33.1.43).
- [47] N. Riley, “Acoustic streaming,” *Theor. Comp. Fluid Dyn.*, vol. 10, pp. 349–356, 1998. DOI: [10.1007/s001620050068](https://doi.org/10.1007/s001620050068).
- [48] M. Van Dyke, *An Album of Fluid Motion*. Stanford, California: Parabolic Press, 1982.
- [49] Y. Bhosale, T. Parthasarathy, and M. Gazzola, “Soft streaming – flow rectification via elastic boundaries,” *J. Fluid Mech.*, vol. 945, R1, 2022. DOI: [10.1017/jfm.2022.525](https://doi.org/10.1017/jfm.2022.525).
- [50] M. Y. Jaffrin and A. H. Shapiro, “Peristaltic Pumping,” *Annu. Rev. Fluid Mech.*, vol. 3, pp. 13–37, 1971. DOI: [10.1146/annurev.fl.03.010171.000305](https://doi.org/10.1146/annurev.fl.03.010171.000305).
- [51] Y. C. Fung and C. S. Yih, “Peristaltic Transport,” *ASME J. Appl. Mech.*, vol. 35, pp. 669–675, 1968. DOI: [10.1115/1.3601290](https://doi.org/10.1115/1.3601290).
- [52] P. Hall, “Unsteady viscous flow in a pipe of slowly varying cross-section,” *J. Fluid Mech.*, vol. 64, pp. 209–226, 1974. DOI: [10.1017/S0022112074002369](https://doi.org/10.1017/S0022112074002369).
- [53] V. Anand and I. C. Christov, “Revisiting steady viscous flow of a generalized Newtonian fluid through a slender elastic tube using shell theory,” *Z. Angew. Math. Mech. (ZAMM)*, vol. 101, e201900309, 2021. DOI: [10.1002/zamm.201900309](https://doi.org/10.1002/zamm.201900309).
- [54] P. S. Ayyaswamy, “Introduction to Biofluid Mechanics,” in *Fluid Mechanics*, P. K. Kundu, I. M. Cohen, and D. R. Dowling, Eds., 6th ed., San Diego, CA: Academic Press, an imprint of Elsevier Inc., 2016, ch. 16, e1–e73. DOI: [10.1016/B978-0-12-405935-1.00016-2](https://doi.org/10.1016/B978-0-12-405935-1.00016-2).
- [55] M. Zamir, *The Physics of Pulsatile Flow*. New York, NY: Springer, 2000. DOI: [10.1007/978-1-4612-1282-9](https://doi.org/10.1007/978-1-4612-1282-9).
- [56] A. H. Shapiro, “Steady flow in collapsible tubes,” *ASME J. Biomech. Eng.*, vol. 99, pp. 126–147, 1977. DOI: [10.1115/1.3426281](https://doi.org/10.1115/1.3426281).

- [57] A. Libai and J. G. Simmonds, *The Nonlinear Theory of Elastic Shells: One Spatial Dimension*. San Diego, CA: Academic Press, 1988. DOI: [10.1016/B978-0-12-447940-1.X5001-6](https://doi.org/10.1016/B978-0-12-447940-1.X5001-6).
- [58] S. B. Elbaz and A. D. Gat, “Axial creeping flow in the gap between a rigid cylinder and a concentric elastic tube,” *J. Fluid Mech.*, vol. 806, pp. 580–602, 2016. DOI: [10.1017/jfm.2016.587](https://doi.org/10.1017/jfm.2016.587).
- [59] X. Wang, S. D. Pande, and I. C. Christov, “Flow rate–pressure drop relations for new configurations of slender compliant tubes arising in microfluidics experiments,” *Mech. Res. Commun.*, vol. 126, p. 104016, 2022. DOI: [10.1016/j.mechrescom.2022.104016](https://doi.org/10.1016/j.mechrescom.2022.104016).
- [60] D. P. Gaver, D. Halpern, O. E. Jensen, and J. B. Grotberg, “The steady motion of a semi-infinite bubble through a flexible-walled channel,” *J. Fluid Mech.*, vol. 319, pp. 25–65, 1996. DOI: [10.1017/S0022112096007240](https://doi.org/10.1017/S0022112096007240).
- [61] J. Peiró and A. Veneziani, “Reduced models of the cardiovascular system,” in *Cardiovascular Mathematics*, ser. Modeling, Simulation and Applications, L. Formaggia, A. Quarteroni, and A. Veneziani, Eds., vol. 1, Milano: Springer, 2009, ch. 10, pp. 347–394. DOI: [10.1007/978-88-470-1152-6_10](https://doi.org/10.1007/978-88-470-1152-6_10).
- [62] A. Updegrave, N. M. Wilson, J. Merkow, H. Lan, A. L. Marsden, and S. C. Shadden, “SimVascular: An Open Source Pipeline for Cardiovascular Simulation,” *Ann. Biomed. Eng.*, vol. 45, pp. 525–541, 2017. DOI: [10.1007/s10439-016-1762-8](https://doi.org/10.1007/s10439-016-1762-8).
- [63] H. Lan, A. Updegrave, N. M. Wilson, G. D. Maher, S. C. Shadden, and A. L. Marsden, “A Re-Engineered Software Interface and Workflow for the Open-Source SimVascular Cardiovascular Modeling Package,” *ASME J. Biomech. Eng.*, vol. 140, p. 024501, 2018. DOI: [10.1115/1.4038751](https://doi.org/10.1115/1.4038751).
- [64] C. Zhu, V. Vedula, D. Parker, N. Wilson, S. Shadden, and A. Marsden, “svFSI: A Multiphysics Package for Integrated Cardiac Modeling,” *J. Open Res. Softw.*, vol. 7, no. 78, p. 4118, 2022. DOI: [10.21105/joss.04118](https://doi.org/10.21105/joss.04118).
- [65] C. J. Morris and F. K. Forster, “Oscillatory flow in microchannels,” *Exp. Fluids*, vol. 36, pp. 928–937, 2004. DOI: [10.1007/s00348-003-0776-9](https://doi.org/10.1007/s00348-003-0776-9).